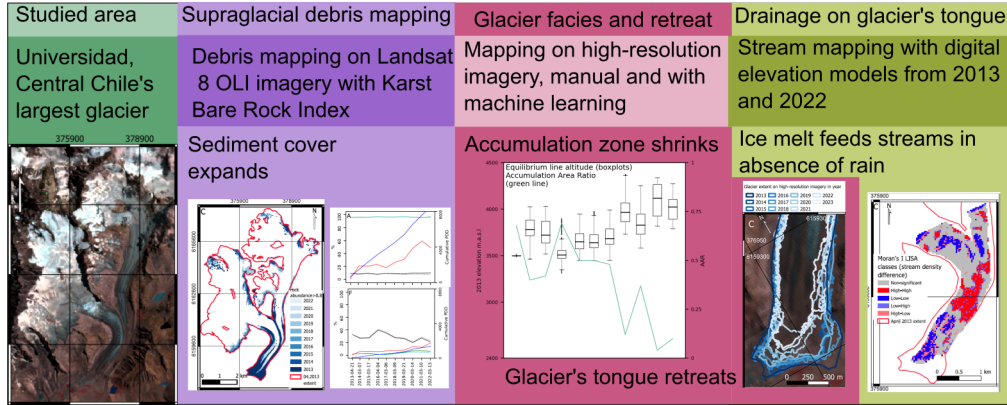


Graphical Abstract

Stable supraglacial hydrology of Universidad Glacier during the central Chile mega drought despite diminishing accumulation zone and significant surface darkening

Julian Podgórski, Michał Pętliski, Alfonso Fernández, Roberto Urrutia, Christophe Kinnard



Highlights

Stable supraglacial hydrology of Universidad Glacier during the central Chile mega drought despite diminishing accumulation zone and significant surface darkening

Julian Podgórski, Michał Pełlicki, Alfonso Fernández, Roberto Urrutia, Christophe Kinnard

- Glacier equilibrium line is rapidly ascending, resulting in a reduction in the extent of firn and leading to the gradual disappearance of the accumulation zone
- Universidad glacier experiences local retreat and expansion of surface debris cover in response to climate desertification
- The Karst Bare Rock Index (KBRI), a spectral index derived from Landsat 8 OLI data and originally designed for karst rock detection, can be effectively employed for mapping debris on the surface of a glacier

Stable supraglacial hydrology of Universidad Glacier during the central Chile mega drought despite diminishing accumulation zone and significant surface darkening

Julian Podgórski^{a,*}, Michał Pętllicki^{b,c,*}, Alfonso Fernández^c, Roberto Urrutia^d and Christophe Kinnard^e

^a*Institute of Geophysics, Polish Academy of Sciences, ul. Księcia Janusza 64, Warsaw, 01-452, Poland*

^b*Jagiellonian University, Faculty of Geography and Geology, Cracow, 30-387, Poland*

^c*Universidad de Concepción, Department of Geography, Concepcion, Chile*

^d*Universidad de Concepción, Centro de Ciencias Ambientales EULA, Concepción, Chile*

^e*Université du Québec à Trois-Rivières, Trois-Rivières, Québec, Canada*

ARTICLE INFO

Keywords:

Andes
Central Chile Mega Drought
debris cover
glacier
glacier hydrology
remote sensing
hyperspectral imagery
LANDSAT
machine learning
OBIA

ABSTRACT

In recent years, Chile has experienced an extraordinary drought that has had significant impacts on both the livelihoods of people and the environment, including the Andean glaciers. This study focuses on analyzing the surface processes of Universidad glacier in central Chile by utilizing multiple remote sensing datasets. We make use of satellite imagery from various sources to accurately track changes in the glacier facies and delineate the glacier margins during the study period. Additionally, digital elevation models from 2013 and 2022 are employed to map the characteristics of the supraglacial drainage system on the glacier's tongue. Our findings highlight the precarious state of the glacier, which serves as a crucial water source for the region. The glacier exhibits locally varied debris accumulation and margin retreat. The most significant impacts are observed on the tongue and secondary accumulation cirques, with the latter at risk of disappearing. Debris cover on the tongue expands, reaching higher elevations, and is accompanied by glacier retreat, especially at higher altitudes. The equilibrium line is rapidly shifting upglacier, although mid-season snow cover tends to reach the 2013 equilibrium line even by 2020. Changes in stream density on the glacier's tongue indicate an increased water supply in this area, likely due to enhanced melting of glacial ice. These observed processes align well with meteorological data obtained from models. The behavior of dust and debris is influenced by precipitation, while the rate of retreat is linked to air temperature.

1. Introduction

Contemporary climate change is profoundly influencing the global cryosphere (Vaughan et al., 2013). Glaciers and Ice Caps are contributing strongly to the sea level rise, despite their small mass, relative to the ice sheets (Zemp et al., 2019). These small ice bodies are predicted to contribute up to 20 cm of sea level rise by 2100, which accounts for approximately 1/6 of what is projected under the most pessimistic climate change scenario (Slangen et al., 2016). Additionally, it is estimated that up to 60% of ice mass loss will occur among the glaciers within UNESCO World Heritage sites (Bosson et al., 2019). Small glaciers not only suffer from the impacts of climate change but also serve as important indicators of its effects. This is evident from the inclusion of snow cover and glaciers on the list of key climatic variables by the Food and Agriculture Organization of the United Nations (FAO) (Schaaf, 2009).

In addition to its purely scientific interest, GIC research holds significant societal relevance. In many regions worldwide, meltwater from mountain glaciers serves as a primary

freshwater source and contributes to hydropower generation (Mark et al., 2015). The thinning of these ice masses poses challenges to people dependent on them (Baraer et al., 2012; Milner et al., 2017; Masiokas et al., 2020). In the Dry Andes, glacier meltwater becomes an important part of the water supply during years with limited snowfall (Masiokas et al., 2020). The loss of ice mass in the region is said to have mitigated societal and economical consequences of the drought for Chile (Dussaillant et al., 2019; Ayala et al., 2020). The 2010-2018 period had a particularly low precipitation in central Chile, sometimes called the Central Chilean Mega-Drought (Garreaud et al., 2019; Kim et al., 2022). The dry conditions have adverse impact on water supply (McCarthy et al., 2022), forests (Venegas-González et al., 2022; Urrutia-Jalabert et al., 2023) as well as on the glaciers of this part of the Andes. In the central region of Chile, drastic recession and disintegration of glaciers was observed between 1955 and 2013 (Malmros et al., 2016). Measurements of the Guanaco glacier, located in north-central Chile, revealed a negative mass balance since 2002 (Kinnard et al., 2020). The glaciers on the Argentinian side of the Andes have experienced consistent mass loss since the middle of the 20th century with a drastic acceleration between 2012 and 2020, a development blamed on the megadrought (Falaschi et al., 2022).

*Corresponding author

✉ jpodgo@igf.edu.pl (J. Podgórski); mpetlicki@udec.cl (M. Pętllicki)

ORCID(s): 0000-0001-5604-3462 (J. Podgórski); 0000-0003-3383-2586

(M. Pętllicki); 0000-0001-6825-0426 (A. Fernández); 0000-0002-6239-9016

(R. Urrutia); 0000-0002-4553-5258 (C. Kinnard)

Melting of ice and snow can occur throughout the entire glacier area. Supraglacial (on the top of a glacier) melt is mainly related to intensity of incoming solar radiation, properties of ice and snow cover, and air temperature (Hock, 2005). Irvine-Fynn and Hubbard (2016) distinguish 3 important hydrological environments on a glacier surface: snow-pack with variable density and water permeability, firn, an aquifer capable of retaining water coming from snow melting at the surface, and bare ice, the least permeable of the three. These facies serve as water storage over different time scales, ranging from snow cover that captures and releases water on a seasonal scale, to retention in glacial ice for centuries (Jones et al., 2019). The properties of bare ice may lead to formation of surface relief forms under flowing water by means of incision and erosion of banks carved into the glacial ice (Benn and Evans, 2010). On temperate glaciers, the stream incision rate often matches or surpasses the ablation rate, and thus stream networks are created anew every melt season (Irvine-Fynn and Hubbard, 2016). The formation of drainage networks commences in the ablation season, after the snow cover of the ablation zone disappears (Fountain and Walder, 1998). The on-glacier river networks assume a dendritic structure and resemble terrestrial river systems, characterized by meandering flows and the formation of pools in areas obstructed by topographic features. Wet ice surface has lower albedo than dry (Ryan et al., 2018), and variable, rough topography enhances melt locally (Cathles et al., 2011). Combination of these two factors leads to increase of melt in areas of high channel densities and thus a feedback is established between accelerating melt and densification of stream network (Pitcher and Smith, 2019).

Brun et al. (2019) listed debris cover as one of the important morphological factors controlling glacier melt in the Himalayas, albeit not as important as slope and mean elevation. A thin cover of debris may increase melt rates (Oerlemans et al., 2009; Basnett et al., 2013), but a sufficiently thick cover of sediments protects the underlying ice from elements and reduces melt (östrem, 1959; Vincent et al., 2016; Jones et al., 2019). Climatic factors of warming and decrease in precipitation were hypothesized to promote expansion of a debris cover on a glacier (Xie et al., 2020). During the megadrought period, a decrease in surface albedo was observed across Chilean glaciers, exhibiting interannual fluctuations, especially in the upper regions of the glaciers (Shaw et al., 2020). In the Dry Andes, glaciers of several classes can be found, from almost clear ice bodies, through debris-covered glaciers to rock glaciers fully covered by a thick layer of debris (Janke et al., 2015).

Research on supraglacial hydrology relies on the availability of data regarding the surface conditions of glaciers. Data from various satellite sensors have been used to map the surface and hydrology of glaciers. For instance, the imagery acquired by a low-resolution MODIS has been employed to map lakes on the Greenland Ice Sheet (Selmes et al., 2011). The surface drainage system of a glacier has been mapped using a medium resolution dataset of Landsat imagery (30 m/pixel) by Wyatt and Sharp (2015), while Smith

et al. (2015) have used high-resolution (2 m/pixel) imagery from the WorldView-2 mission to map drainage on parts of the Greenland Ice Sheet. Additionally, a study on sub-pixel glacier classification by Yousuf et al. (2020) demonstrated the potential of spectral signatures, which are reflectivity patterns characteristic of specific surface types, for mapping different ice facies. The detection of diverse surface types on satellite imagery often employs spectral indices, which establish relationships between the reflectivity of surfaces at different wavelengths to generate maps of specific features. Wessels et al. (2002) have employed the ASTER sensor (15 m/pixel) and several band-ratio indices to map supraglacial lakes in the Mount Everest area. Furthermore, Li and Sheng (2012) proposed an algorithm for glacial lake delineation based on the Normalized Difference Water Index (NDWI) band-ratio tailored to detect water on images Gao (1996). Similarly, Yang and Smith (2013) utilized the same index to detect active meltwater streams on the surface of an outlet glacier of the Greenland Ice Sheet.

Band ratios are a valuable tool for mapping debris-covered glaciers. Shokory and Lane (2023) employed custom spectral indices and Landsat 8 OLI/TIRS imagery, utilizing the panchromatic, thermal infrared, and blue bands, to detect sediment on the glacier surface in the Afghan Hindu-Kush region. A ratio of Near Infrared (NIR) and Shortwave Infrared (SWIR) bands has been successful in identifying exposed ice (Haireti et al., 2016). In a mapping workflow for a group of Chinese glaciers, Haireti et al. (2016) incorporated a ratio of Thematic Mapper bands 4 and 5 which cover near infrared (NIR) and short-wave infrared (SWIR) to detect clean ice areas. These same images were also utilized for glacier outline delineation (Bhardwaj et al., 2014). Additionally, Fleischer et al. (2021) used a band-ratio index of the NIR and SWIR bands from Landsat to detect clean-ice sections of glaciers and observed an upward migration of debris coverage on glaciers in the Alps.

The NIR and SWIR bands are inputs to a Karst Bare Rock Index (KBRI) proposed by Pei et al. (2018) for detection of exposed bedrock in karst landscapes. It uses bands 5 (NIR) and 6 (SWIR) of Landsat 8 OLI instrument in a formula of normalized differential index modified by inclusion of square root in the denominator to improve contrast. To date, KBRI has been used for its intended purpose of mapping desertification in areas underlain by carbonate rocks (Alevkayali et al., 2023; Pu et al., 2021), as well as in the role of a reference method for the development of remote sensing products (Ruan et al., 2023; Sales et al., 2023). In this work, we want to test the ability of the KBRI index to map a glacier debris cover.

Object-Based Image Analysis (OBIA) is a paradigm of work with raster data that relies on segments identified within the image (Blaschke et al., 2014). Each segment can be characterized by statistics of the pixel populations included within, including means, minima, and maxima of reflectivities or image textures. This allows for a richer set of properties for analysis compared to pixel-based image analysis, where only band reflectivities and values of spectral

indices from each individual pixel can be utilized. This is particularly advantageous for machine learning (ML) algorithms, as they generally perform better with a larger number of independent variables, albeit careful variable selection is required to avoid overfitting (Chen et al., 2020). In glaciology, OBIA has been used to map debris-covered glaciers (Rastner et al., 2014; Robson et al., 2015), glacial lakes (Mittkari et al., 2017) and iceberg detection (McNabb et al., 2016). The object-based approach was also combined in the past with ML for studies of lacustrine icebergs (Podgórski and Pełlicki, 2020), mapping of glaciers in the Arctic (Ali et al., 2023), and in Pamir (Lu et al., 2020).

In this work, we present ten years of evolution of the debris cover on Universidad Glacier. We use high-resolution hyperspectral image to create a model for detection of the glacier's debris cover in Landsat 8 OLI pixels. We present maps of glacier facies derived from the application of object-based image analysis and machine learning, as well as a timeseries of changes of snowpack extent and equilibrium line altitude (ELA). Furthermore, our objective is to ascertain whether the observed alterations in albedo, as documented in prior studies, align with the presence of increased sediment deposition or if they are exclusively attributable to the diminishing extent of snow cover and the retreat of the glacier. We complete the analysis of Universidad Glacier's hydrology with a discussion of the state of supraglacial stream networks in 2013 and 2022.

2. Study Area

Universidad glacier is located in Chile, approximately 130 km south of the country's capital, Santiago, in the Dry Andes near the Chile-Argentina border (Fig. 1A). It is a valley glacier with a notable elevation range, spanning from 2450 to 4550 m a.s.l. With a surface area of over 27 km² (Kinnard et al., 2018), it is also the largest glacier in Chile north of the Patagonian Icefields. Observations by Lliboutry (1958) have documented various features on the glacier's surface, such as glacier mills and ogives. The glacier was classified as Maritime ("Temperate" according to modern classification). As the Chilean Andes are experiencing a consistent warming since at least 1979 (Falvey and Garreaud, 2009), the presence of cold ice is not expected in the area.

During the hydrological year 2012/13, the measured glaciological mass balance of Universidad Glacier was -0.32 ± 0.40 m w.e. a⁻¹. However, in the following year 2013/14, the negative mass balance increased to -2.53 ± 0.57 m w.e. a⁻¹. This abrupt change was attributed to a combination of factors such as the amount of snowfall, surface albedo and cloud cover (Kinnard et al., 2018). A study based on satellite digital elevation models (DEMs) showed a long-term mass loss rate of 0.44 ± 0.08 m w.e. a⁻¹ during the period of 2000-2013 (Podgórski et al., 2019). In the immediate vicinity of the Universidad glacier, there was a moderate mass gain observed between 2000 and 2009, followed by a period of intensive mass loss (Dussaillant et al., 2019).

Recently, a study of local geomorphology has shown advances of the glacier to a maximum extent in the 13th to 16th centuries and later in the mid-19th century, followed by gradual demise up until today (Fernández-Navarro et al., 2023). In addition, a model of the glacier's deicing was developed to show the evolution of periglacial topography from a clean glacier through increasing debris accumulation to an ice-cored moraine and dead ice situation (Fernández et al., 2022).

During droughts and dry summers, the glacier's meltwater can be an important source of water for the inhabitants of densely populated central Chile (Valdés-Pineda et al., 2014). One of the important rivers for Chilean water resources is Tinguiririca river, partially fed by the Universidad Glacier that sits on the headwaters of the San Andrés tributary (Kinnard et al., 2018). An estimate showed that up to 20% of flow in the river basin in 2010 was contributed by Universidad meltwater (Bravo et al., 2017). Studies of Universidad's hydrology can, therefore, bring not only scientific benefits but also provide informative insights for local resource management.

In our work we analyze several places on Universidad glacier, manually picked to represent different environments. These regions of interests (ROIs) are mapped on Figure 1B and the mean elevation in m.a.s.l. is listed in the legend box of the map.

3. Materials and Methods

3.1. Dataset description

An airborne hyperspectral radiance image served as a basis for establishment of a mathematical model for recalculation of KBRI values to detected rock abundance. The image was acquired on 23 April 2013, with a HySpex VNIR-1600 camera. The image covers the lower tongue of the glacier and the upper part of the main trunk of the glacier (Fig. 1C). The image has 160 spectral bands, of which we used 120 due to noise in the infrared bands (above 850 nm).

We used two digital elevation models in this study. The first one was acquired during the same measurement campaign as the hyperspectral dataset. The model is based on airborne laser scanning with a Riegl LMS-Q560 laser scanner mounted on the airplane. The original resolution of this DEM is 1 m. It was described in more detail in a previous work on Universidad's elevation change (Podgórski et al., 2019). The second DEM is an UAV-imagery based product acquired on 12 March 2022. It was acquired with an EbeeX fixed-wing UAV equipped with an onboard double frequency GNSS receiver. The post-processing kinematic method was used to georeference the images to centimetric accuracy using a local GNSS base. The photogrammetric solution was calculated in Pix4d software, yielding a DEM with a 5 cm/pixel spatial resolution. This product was then resampled to 1 m/pixel to bring it to agreement with the earlier DEM.

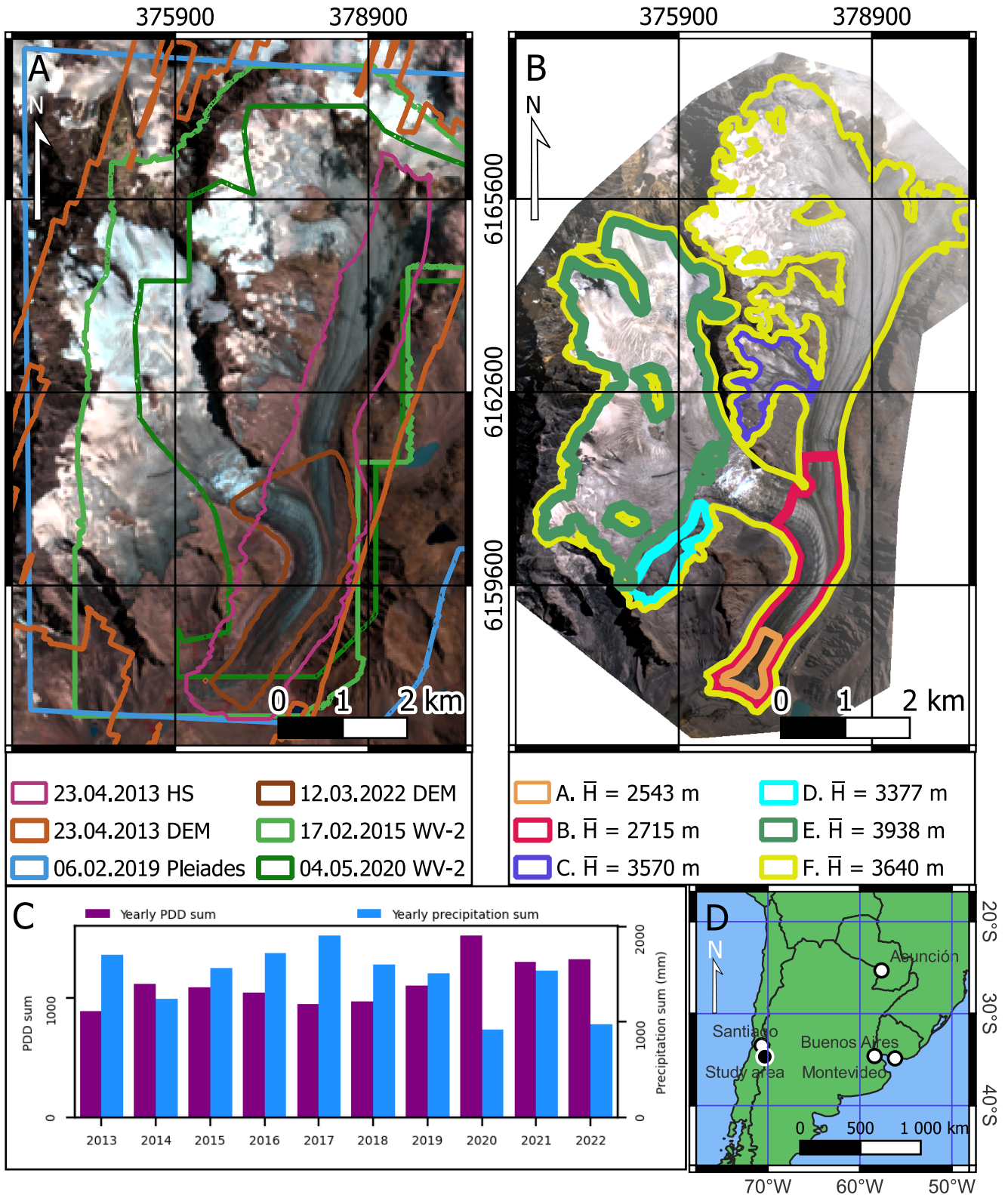


Figure 1: Overview of the study area. A – Extents of the used high-resolution datasets on the background of the 03.02.2023 Landsat 8 true color image of the Universidad Glacier; B – Localization and extents of the custom Regions of Interest chosen for analyses throughout this paper on the background of the 30.03.2022 Dove image of the Universidad Glacier. Letters in legend correspond to letters on maps and plots in the later parts of the article. Numbers alongside letters in legend indicate mean 2013 elevation in meters; C – Yearly PDD sum and precipitation sum timeseries for the study period sourced from the ERA5-Land model. D – study site location within the central part of South America.

Table 1

Summary of imagery used in the study. BOA stands for Bottom of the Atmosphere, while TOA for Top of the Atmosphere. DEM stands for Digital Elevation Model.

Sensor	Number of bands	Spatial resolution (m/pixel)	Processing level	Acquisition times
Airborne datasets				
Riegl LMS-Q560	1 (elevation)	1 m/pixel	DEM	23.04.2013
EbeeX UAV DEM	1 (elevation)	5 cm/pixel resampled to 1 m/pixel	DEM	12.03.2022
HySpex VNIR-1600	160	1 m/pixel	at-sensor radiance	23.04.2013
Satellite datasets				
PS2	4	1 m/pixel	TOA radiance	2017, 2018
PS2.SD	4	1 m/pixel	TOA radiance	2019-2021, yearly
PSB.SD	8	1 m/pixel	TOA radiance	2022, 2023
RapidEye-1	4	3 m/pixel	TOA radiance	2014-2016, yearly
Pleiades	4	0.5 m/pixel	BOA reflectance	06.02.2019
WorldView-2	8	0.5 m/pixel	BOA reflectance	17.02.2015, 04.05.2020
Landsat 8 OLI	7	30 m/pixel	BOA reflectance	2013-2023, yearly

We have acquired WV-2 and Pleiades images as Orthorectified 2A level datasets, radiometrically and geometrically corrected (DigitalGlobe, 2016). RapidEye-1 were acquired as the level 1B (basic analytic) Top of Atmosphere (TOA) radiance non-orthorectified products. In addition to that, we used imagery from Dove satellites, which are part of the PlanetScope constellation. The images were taken with PS2, PS2.SD and PSB.SD instruments, and were acquired as orthorectified TOA radiance images at the 3B (analytic) processing level. Considering the diversity of instruments and the common purpose of these images, we will refer to them as Dove images hereafter. We applied atmospheric correction to the WV-2 and Pleiades images using the AT-COR algorithm (Richter and Schläpfer, 2017), and then pansharpened the images. The imagery from WV-2, RE-1 and Pleiades was orthorectified with the PCI Geomatica software, with the ASTER Global Digital Elevation Model v003 (NASA/METI/AIST/Japan Space Systems And U.S./Japan ASTER Science Team, 2019) used as a source of a generalized reference model for terrain.

For the long-term detection of debris cover we have used reflectance images from the Operational Land Imager (OLI) instrument mounted on the Landsat 8 satellite. We used Google Earth Engine (Gorelick et al., 2017) and Google Colaboratory on-line platform to source, filter and process the OLI images with Python programming language. We manually selected one image per year from 2013 to 2023, prioritizing cloud- and snow-free scenes typically captured in late summer, ie. March or April.

Hourly air temperature (T) and precipitation (P) above the glacier tongue were extracted from the ERA5-Land hourly reanalysis (Muñoz-Sabater, 2019) in GEE. We have downloaded the hourly air temperature and precipitation from the model cell that covers Universidad glacier. For the ROI-based analyses, we adjusted the temperature time series to better align with the mean elevation of each specific ROI, instead of using the fixed elevation of a model cell.

To achieve this, we applied a temperature gradient of $-0.006^{\circ}\text{C}/\text{m}$ based on Bravo et al. (2017). This gradient includes a constant value of $-0.006^{\circ}\text{C}/\text{m}$ during nighttime and a generalized elevation lapse rate of $-0.006^{\circ}\text{C}/\text{m}$ during the day, representing the mean value between the extremes of $-0.007^{\circ}\text{C}/\text{m}$ and $-0.005^{\circ}\text{C}/\text{m}$ mentioned by the authors. For each ROI, we used the temperature time series adjusted for elevation to calculate Positive Degree Days (PDD), which serves as a proxy for glacier ice melt. We calculated both the PDD and cumulative PDD for the periods between April 1st and March 31st for each year from 2013 to 2022 (Fig. 1B). In addition to the meteorological data, we have acquired information about water discharge in the Tinguririca river, the river fed by Universidad's meltwater. Mean monthly discharge values were obtained from the Chilean General Water Directorate database. The data come from the gauge station located near La Virgen village, approximately 57 km downstream from the glacier terminus along the river course. In 2023, there were two run-of-river hydropower generation installations located between the glacier and the gauging station. It is worth noting that neither of these installations creates artificial lakes. As a result, we assume that the discharge record obtained from the gauging station represents the natural flow of the river.

3.2. Mapping glacier's ice facies

We segmented the pre-processed Pleiades and WV-2 images using the multiresolution segmentation algorithm of eCognition 10.2 (Trimble Geospatial, 2017). The segmented images were then classified with the Random Forest supervised classification algorithm. We manually selected polygons as training data based on visual interpretation of glacial features. Each image required a distinct training set due to significant differences in lighting conditions. Classification of all images included the following classes:

- "ice" for exposed glacial ice

- "blue ice" for segments of deep, non-metamorphised glacial ice exposed in crevasses
- "dark ice" for exposed ice with embedded sediments, most often found on the Universidad's tongue
- "snow/firn" for areas of snowpack and exposed firn, as the two are not distinguishable on the available imagery
- "rock" for rocks surrounding the glacier and debris accumulated on the glacier's surface
- "deep shadow", a class intended to filter out darkest shadows so that they do not pollute other classes' training and results
- "glare" for very bright areas, saturated with solar glare, found only on the 2020 WV-2 image.

The properties used for segment classification were the means of all image bands, as well as the means of several spectral indices, and four Haralick texture measures: Angular 2nd momentum, Entropy, Contrast, and Standard Deviation (Haralick et al., 1973).

3.3. Manual detection of ELA and AAR

In addition to the supervised classification, we have manually digitized outlines of the glacier and estimates of Equilibrium Lines on the high-resolution satellite imagery. We used Dove, WV-2, RE-1 and Pleiades imagery to draw the outlines of the glacier in the subsequent years. We manually traced the edge of the glacier within the eCognition 10.2 program using segmented multispectral imagery. This process considered the demarcation between the debris-covered ice and the surrounding valley slopes or sediment-covered areas resulting from glacier recession. The outcome of this effort was a set of 11 polygons representing the glacier extent for the years 2013-2023. The equilibrium lines were digitized as the lower edge of the snow presence, as visually identified in the image. We compared the ELA values with seasonal (3-month) Oceanic Niño Index (ONI) values for winter (June, July, August, JJA) and summer (December, January, February, DJF) sourced from NOAA (NOAA, 2023). This value served as a proxy of the El Niño Southern Oscillation (ENSO) stages. We calculated Spearman correlation between ELA, summer ONI and previous year's winter ONI, and determined the correlation's significance with a permutation test.

3.4. Mapping sediment cover on the hyperspectral image

We generated a rock abundance map that represents the proportion of rock material within each pixel across the section of the glacier covered by the hyperspectral (HS) data. This includes both sediment accumulating on the glacier's surface and sections of rock exposed due to the glacier's retreat. Two land cover classes were defined for detection on the hyperspectral (HS) image: bare ice and bare rock. To create a spectral library, we manually selected reference

pixels (endmembers) for each class from within the HS image. Each endmember corresponds to one of the classes and represents either bare, exposed ice or a pixel with 100% coverage of rock or debris, such as mountain slopes or moraines. The selected endmembers within each class exhibit diverse spectral characteristics and were included in the library. For the unmixing task, we used MESMA (Multiple Endmember Spectral Mixture Analysis) instead of simple linear unmixing, as MESMA can handle multiple endmembers per class (Roberts et al., 1998). We employed an implementation of MESMA specifically designed for the Quantum GIS software program (Crabbé et al., 2020).

The outcome of this process was a map indicating the contribution of ice and sediment to the radiance curve of each pixel. Furthermore, the selected MESMA implementation incorporated a third category called "Shade," which accounted for the influence of varying lighting conditions on the appearance of areas covered by identical materials. The final classified product is normalized to remove the "Shade" class. Percentages of "Ice" and "Rock" classes are adjusted so that they sum to 100% while retaining the original proportionality of "Ice" to "Rock" abundances.

3.5. Mapping debris cover with Landsat imagery

We used the averaging algorithm provided by the GDAL package (GDAL_Average) to aggregate the rock abundance map based on the hyperspectral image to the resolution and grid of the OLI imagery. To devise a method to map the debris cover, we paired HS data with a map of KBRI index created with OLI imagery. We selected an OLI scene closest in time to the HS acquisition for the calibration of the model. The selected OLI image was taken on 21 April 2013, 2 days before the HS image. Meteorological data obtained from the ERA5-Land model indicate that there was no precipitation or snow events recorded in the area of Universidad during the time period between the two image acquisitions. Therefore, we assume that the two images are comparable in terms of meteorological conditions.

The Karst Bare-Rock Index (KBRI) introduced by Pei et al. (2018), was used as a proxy to assess the presence of rock material on the surface of and around the glacier. The index is calculated with the Formula 1:

$$KBRI = \frac{\rho_{SWIR1} - \rho_{NIR}}{20\sqrt{\rho_{SWIR1} + \rho_{NIR}}} \quad (1)$$

where ρ stands for surface reflectance of the indicated OLI band. We assumed that the selected OLI image depicts a situation identical to that imaged by our hyperspectral image and compared the KBRI scores with the debris coverage map. To establish a relationship between OLI KBRI values and debris coverage, we fitted a generalized logistic curve to the data. This curve provided a model for converting OLI KBRI values to debris coverage. Using this model, we calculated the debris coverage for each OLI image in our time series. We used image segmentation to detect regions with high and low debris coverage, including moraines and areas completely covered by dirt. Additionally, we identified

areas without sediment material, such as bare ice and snow. We ran Accelerated Hierarchical Density-Based Clustering Algorithm (HDBSCAN, McInnes and Healy (2017)) unsupervised machine learning algorithm (an extension of the DBSCAN algorithm (Campello et al. (2013))) on the KBRI-derived sediment cover maps to perform 3D clustering. We converted the clustered data to vector maps and used them to study the expansion of debris cover during the 2013–2022 period. For the glacier’s footprint, we utilized the manually traced outlines of Universidad’s extent on the high-resolution hyperspectral (HS) image.

Besides the KBRI, we also calculated a broadband albedo using the same OLI imagery. To derive the Landsat OLI albedo, we employed the formula devised by Liang (2001):

$$\alpha_{OLI} = 0.356\rho_{blue} + 0.130\rho_{red} + 0.373\rho_{NIR} + 0.085\rho_{SWIR1} + 0.072\rho_{SWIR2} - 0.018 \quad (2)$$

where ρ stands for pixel’s reflectivity in the indicated bands.

Within each ROI we calculated the following timeseries:

- Rock abundance and albedo within the entire ROI,
- Percentage of non-glacier surface within the ROI – this measure is a measure of retreat of the glacier.
- Rock abundance and albedo on the area intersecting the ROI and the manually digitized glacier contour to discern processes occurring on the glacier surface from the generalized signal coming from the entire ROI
- Annual and cumulative PDD computed with elevation-corrected ERA-5 Land temperatures

To analyze the relationships between the various measures of surface darkening or glacier retreat and the meteorological variables obtained from the ERA5-Land model, we constructed Spearman correlation matrices for each of the ROIs. We chose to use the Spearman coefficient due to the significant non-normality of the rock abundance distributions within the ROIs. To determine the statistical significance of these correlations, we performed a permutation test using the scikit-learn Python library.

3.6. Drainage network on the glacier’s surface

With the use of the 2013 and 2022 DEMs, we generated maps of streams in the lower section of the glacier’s tongue. The extent of the stream map is constrained by the extent of the more limited 2022 DEM. In order to accurately include glacial wells in the drainage system mapping, we created a well map by identifying local depressions in the elevation models. We used the PCRaster plugin (Karssenberget al., 2010) in QGIS 3.28 software to generate Local Drain Direction (LDD) maps for both DEMs. The wells map was employed as a representation of water sinks for this purpose. Using this information, we derived maps of stream orders, which served as the basis for the general stream network

map. In order to remove data artifacts, streams with a length of 1 m or less were filtered out from the final map.

We used square polygons aligned with the Landsat 8 pixel grid to derive stream density (m/m^2) and mean stream order. Afterwards, we have calculated Moran’s I Local Index of Spatial Association (LISA) using the difference maps as inputs to search for local changes between 2013 and 2022. For Moran’s I LISA we used the GeoDa software (Anselin et al., 2006; Anselin, 2018). The results included maps of the LISA value, which represents the statistical significance of clustering compared to a random spatial distribution of values. Additionally, the data was classified into interpretative classes based on clusters of high/low differences, including the High-High and Low-Low classes. Furthermore, local outliers from the clusters were classified, such as the High-Low class representing spots of high change surrounded by areas of low change, and the Low-High class representing low-change points within high-change environments.

4. Results

4.1. Multispectral mapping of facies

The "snow" class represents areas covered by a smooth, very bright, white surface. This class includes both snow and firn, as they were visually and algorithmically indistinguishable from each other. In the upper reaches of the glacier, snow or firn penitentes were observed. The "fresh ice" class, trained to detect blue-tinted ice exposed within icefalls, also appears on bright objects in the highest parts of the accumulation zones, emphasizing the spectral similarity between the bright species of snow and ice (Fig. 2).

The extent of the snow-firn cover varies and does not exhibit a clear trend of recession or advancement between years. However, locally, the mid-season snowline reaches the 2013 equilibrium line altitude (ELA) of approx. 3500 m.a.s.l. established with mass balance-elevation relationships (Kinnard et al., 2018). Despite being visually colored by a layer of sediment dust, the snow cover is easily distinguishable from the surrounding rocks and the accumulated supraglacial sediment cover.

The sequence of multispectral classifications shows a gradual darkening and expansion of sediment cover on the glacier’s tongue (Fig. 2). The high-resolution imagery allowed us to distinguish between the dark ice of the ogive bands and the actual accumulation of sediment. The high resolution images show trends of an increasing build-up of sediment on the glacier’s tongue, with a strip of still-exposed ice present in the eastern part of the tongue. The margins of the western accumulation zone and the two small accumulation basins were correctly classified as rock material, not darkened ice. Gradual narrowing of the ice outlets from the small cirques to the glacier’s main trunk is visible on the WV-2 and Pleiades imagery (Fig. 2).

A notable feature of the collection of maps is the distinctiveness of the 2020 WV-2 classification, particularly in its extensive coverage of the "glare" class in the upper parts of the glacier and large swaths of deep shadow (Fig. 2C).

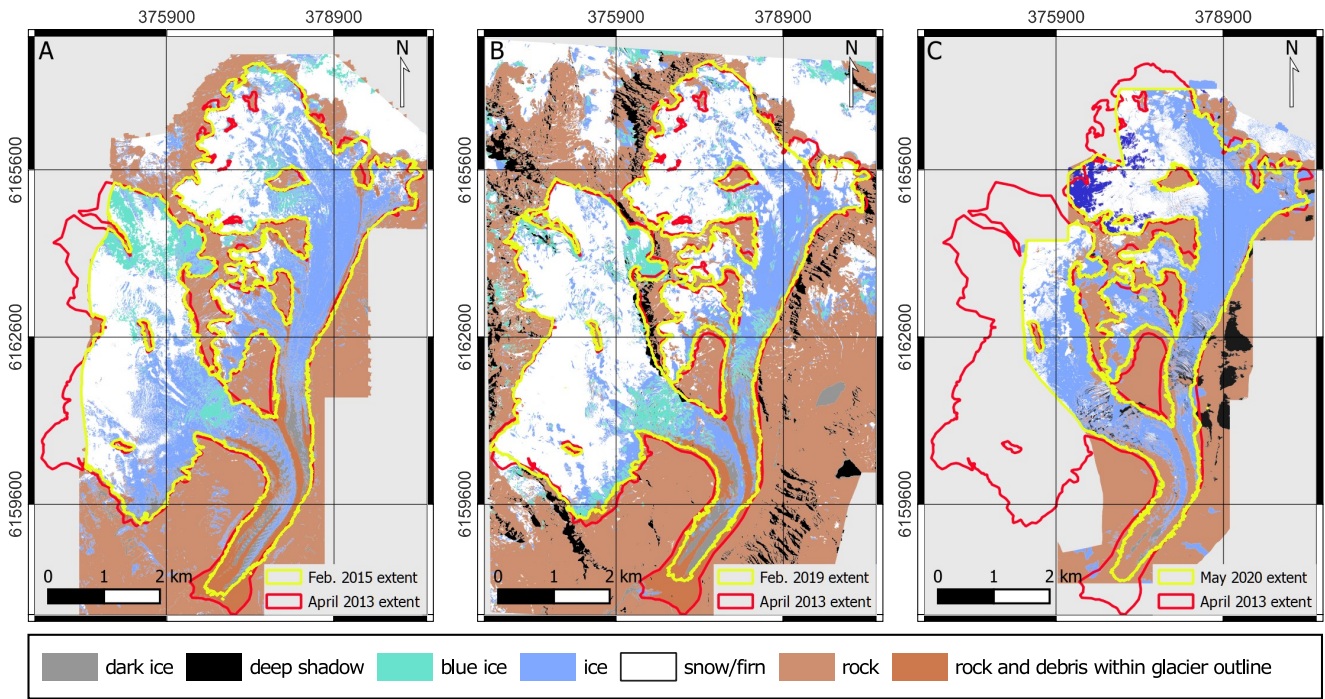


Figure 2: Surface cover type on Universidad glacier determined through object-based classification of high-resolution multispectral satellite imagery. A – WorldView-2 image, 17.02.2015; B – Pleiades image, 06.02.2019; C – WorldView-2 image, 04.05.2020.

This image required a slightly modified training approach for the machine learning classifier to account for the significant brightness differences between areas exposed to direct sunlight and those covered by shadows. As a result, the "dark ice" class was merged with "ice" class in the image.

4.2. Manual mapping

The ELA, as traced by the extent of snow/firm cover, has increased over the years (Fig. 3 and 4A). The 2013 ELA of 3500 m.a.s.l. was surpassed by over 200 meters the following year and remained above 3700 m.a.s.l. until 2023, except for the period from 2016 to 2018. During this period, the snow cover retreated up 3526 ± 93 m.a.s.l. in 2016 and above 3660 m.a.s.l. in 2017 and 2018 (Tab. 2). In 2020, the ELA exceeded 4000 m.a.s.l. (4009 ± 173 m.a.s.l.) for the first time, and the AAR dropped to 0.12.

The reduction in the AAR corresponds to the diminishing extent of snow/firm cover (Fig. 4A). While the AAR was 0.68 in 2013, it dropped below 0.5 as early as 2014, exhibiting similar trends to the changes in ELA. The AAR experienced a fluctuating decrease with a temporary increase between 2016 and 2018. By 2023, the AAR reached 0.10, which is less than one-fifth of its initial value in 2013 (Tab. 2). The year with the highest ELA and the lowest AAR was 2022. During this year, the lower edge of the snow extent reached an elevation of 4105 ± 69 m.a.s.l. resulting in only 4% of the glacier's area remaining in the accumulation zone.

Of the four Spearman correlations computed between ELA, AAR, and ONI for summer and previous year's winter, only one value is statistically significant. There is a significant correlation between the AAR and the previous year's

Table 2

Equilibrium Line Altitude (ELA) and Accumulation Area Ratio (AAR) of Universidad glacier in 2013-2023. The values are based on manual delineation of the equilibrium line in optical satellite imagery for years 2014-2023, whereas for year 2013 the value reported by Kinnard et al. (2018) with no error bounds is provided. The two rightmost columns list 3-month ONI values for summer and previous year's winter.

Year	ELA $\pm 1\sigma$ (m.a.s.l.)	AAR	ONI Summer (DJF)	ONI winter (JJA, previous year)
2013	3500	0.68	-0.40	0.20
2014	3797 ± 121	0.40	-0.40	-0.40
2015	3756 ± 138	0.42	0.50	0.00
2016	3526 ± 93	0.69	2.50	1.50
2017	3661 ± 110	0.50	-0.30	-0.40
2018	3669 ± 108	0.50	-0.90	0.10
2019	3710 ± 110	0.48	0.70	0.10
2020	4009 ± 173	0.12	0.50	0.30
2021	3853 ± 141	0.37	-1.00	-0.40
2022	4105 ± 169	0.04	-1.00	-0.40
2023	4007 ± 120	0.10	-0.70	-0.80

winter ONI, with a coefficient of 0.60. The remaining correlation pairs exceed the significance threshold of $p > 0.05$, and the correlation values themselves were low. The correlations of ELA were -0.43 and -0.48 with the summer ONI and the previous year's winter ONI, respectively. The AAR was correlated with the summer ONI at 0.50.

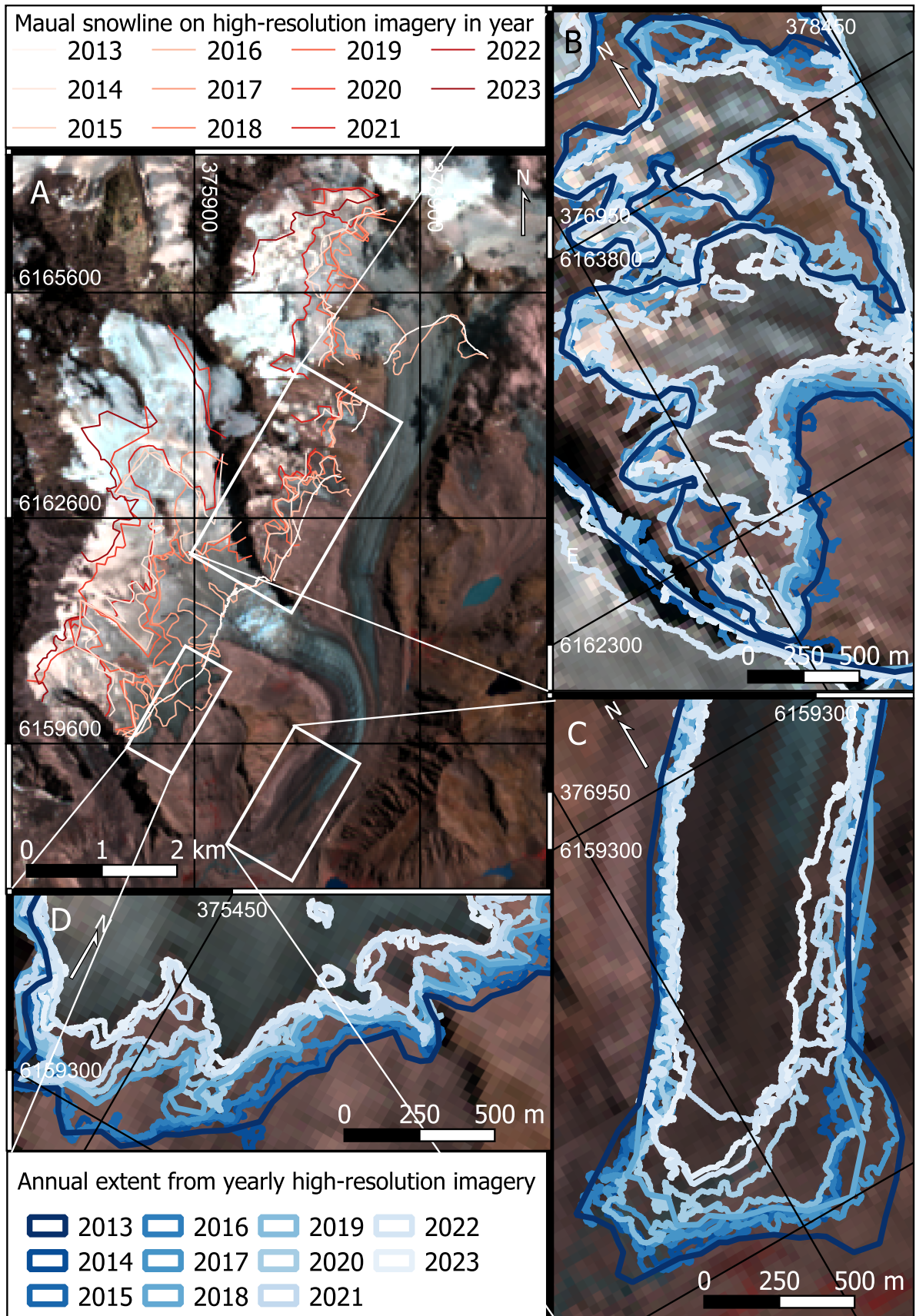


Figure 3: Results of manual glacier extent digitizing on high-resolution Dove satellite imagery. A – overview of Universidad with manually traced snow extent in each year; B – shrinking of the small cirques; C – Recession of the glacier’s tongue; D – Recession of the glacier in the south-eastern part of the western accumulation zone.

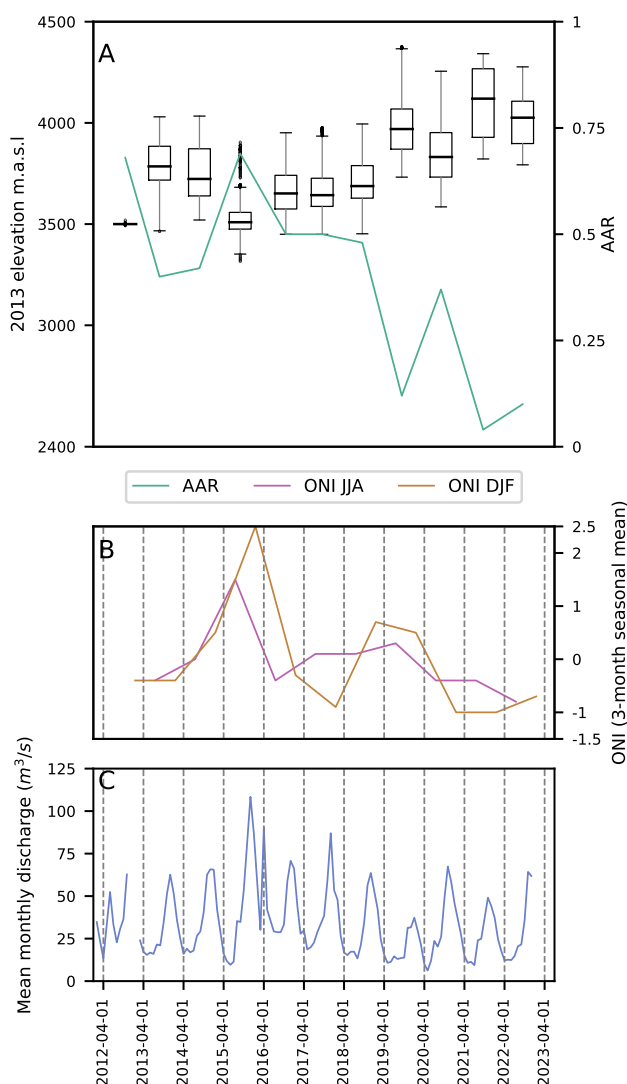


Figure 4: ELA, AAR and ONI changes compared to hydrological record of Tinguririca river. A – ELA values with 1σ error bars (black boxplots), and AAR values in each year (green line); B – ONI seasonal values for winter (brown) and summer (violet); C – Mean monthly discharge measured in Bajo los Briones gauge station. Note vertical lines on panels B and C, indicating the end of hydrological year on 1 April of each year.

4.3. KBRI-sediment cover model

Over the area covered by the hyperspectral image, the KBRI values consistently remain negative, regardless of the rock abundance within pixels (Fig. 5). The relationship between hyperspectral rock abundance and OLI KBRI generally follows a linear pattern in the middle section but exhibits wide clusters of points near the extremes (0 and 100%). Notable deviations from the linear pattern can be observed at both extreme ends, with distinct ranges of KBRI values extending beyond the main cluster of value pairs. Additionally, irregular shapes can be observed in the point clusters between the KBRI ranges of -0.025 to -0.015 and -0.005 to 0. The logistic curve provides a good fit to the dataset, capturing both the linear-like trend observed in the

intermediate values of debris cover and the wide ranges of L8 KBRI values assigned to MESMA pixels that are either fully covered with rock material or not rocky at all (Fig. 5).

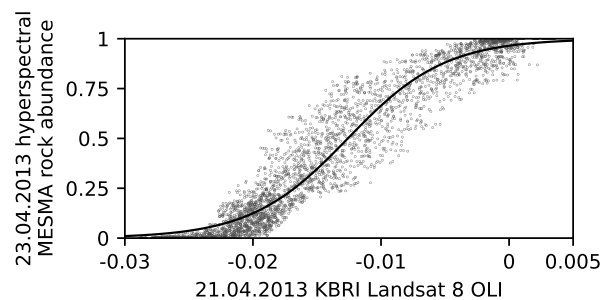


Figure 5: Logistic regression model of relationship between the sediment coverage of hyperspectral pixels and the value of Landsat 8 OLI KBRI.

4.4. Evolution of sediment cover

On the scale of the entire glacier, we found a visible increase in sediment coverage and glacier shrinkage over time (Fig. 6). In 2013, the only noticeable features on the otherwise bright ice surface were medial and lateral moraines in the lower part of the tongue, along with patches of darkness in the western accumulation zone (Fig. 6A). In 2022, on the other hand, multiple zones of continuous sediment coverage can be observed on the tongue, along the sides of the trunks, and at the edges of accumulation zones (Fig. 6B). Most notably, the southern section of the western accumulation field and the smaller cirques to the west of the glacier's main trunk show a decrease in the bright area. Across the 2013–2022 period, there is a gradual expansion of sediment-covered areas and recession of the glacier's tongue in these regions, as observed on the segmented Landsat 8 sediment cover maps (Fig. 6C).

4.5. Rock abundance analysis within the ROIs

The distributions of detected rock abundances within pixels are highly asymmetric, with mean and median significantly different in all cases. This renders the mean an unreliable measure for assessing the overall presence of rock material within a ROI. The median offers a more intuitive representation by indicating that at least half of the pixels (and thus, half of the area) in the ROI contain rock abundance equal to or greater than the median value.

Gradual increase in detected rock abundance is seen in each of the ROIs (Fig. 7). The change is most pronounced on the glacier's tongue and in the small cirque located west of the glacier's main trunk (Fig. 7A, B, C). In the lowest part of the glacier's tongue, the median rock abundance is consistently high throughout the studied period. With the exception of 2021, more than 65% and up to 86.5% of pixels within the ROI exhibit rock abundance levels exceeding 95%, and debris-free pixels (0% rock abundance) are completely absent. The shrinking of the exposed ice area is evident in the gradual narrowing of the boxplot (Fig. 7A). The sub-icefall

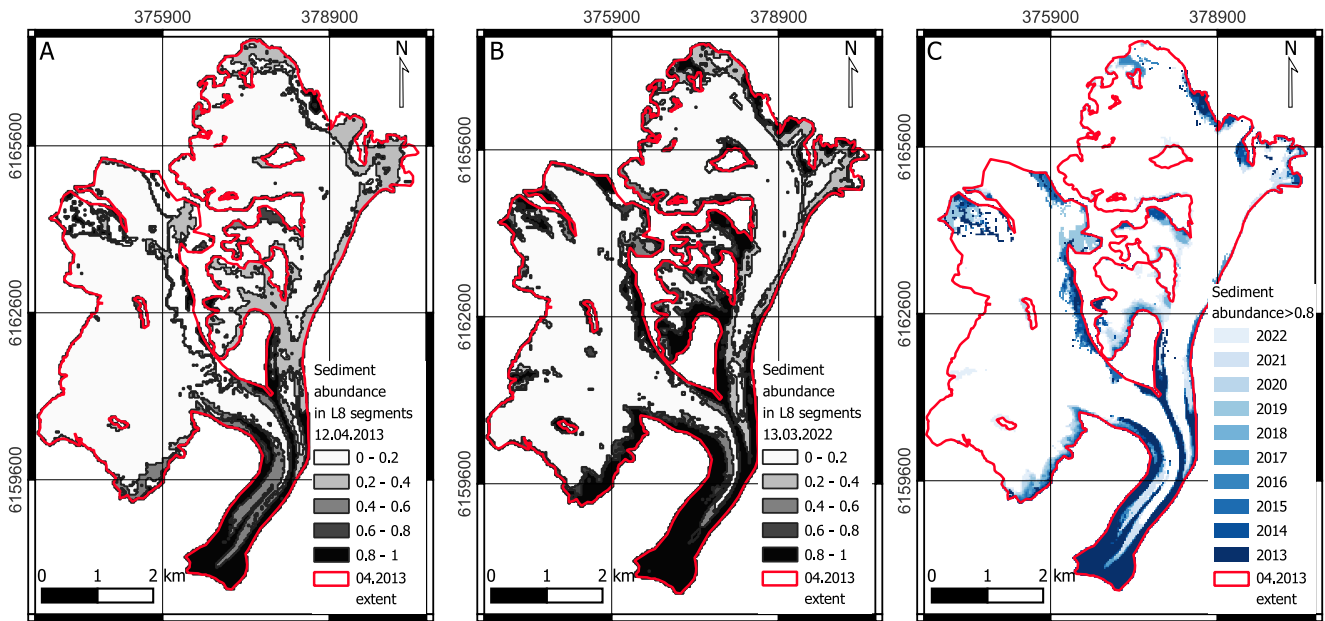


Figure 6: Segmented Landsat 8 maps of rock abundance of Universidad glacier. A – rock abundance on 12.04.2013; B – rock abundance on 13.03.2022; C – segments with sediment coverage higher than that observed between the years 2013-2022 overlaid to illustrate the expansion of high-rock abundance areas over time.

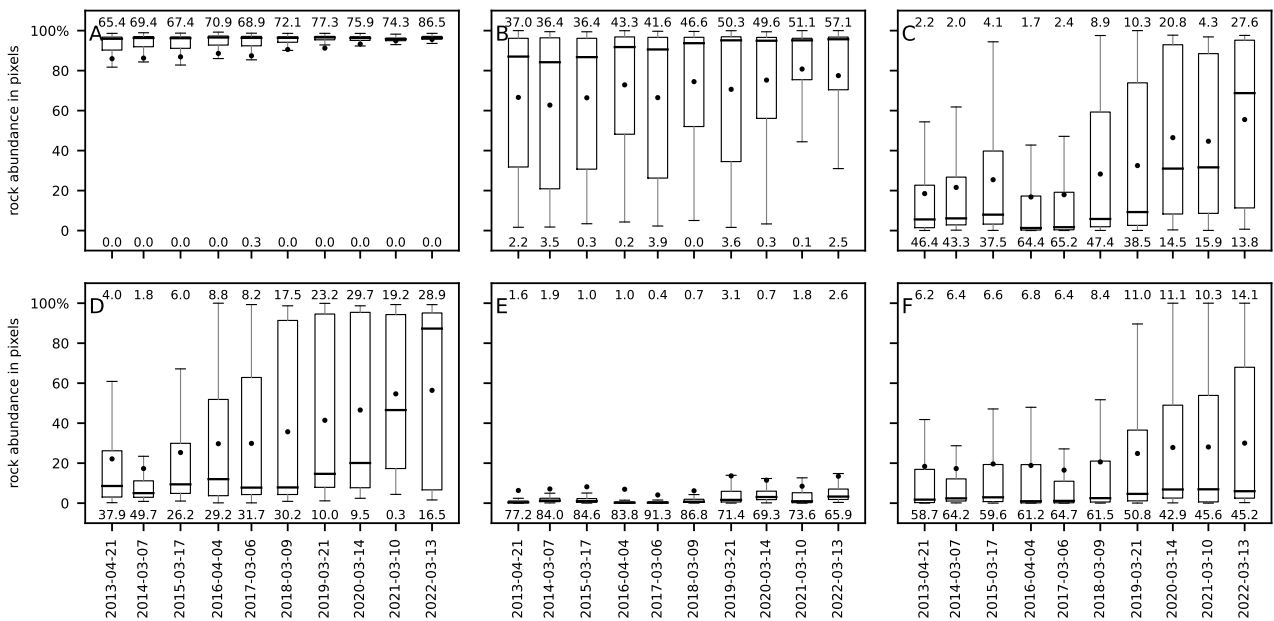


Figure 7: Progression of rock abundance values within entire ROIs (in-ROI rock abundance). Midlines of boxplots indicate median values, black dots - mean values. The numbers above and below each box indicate the percentage of pixels with more than 95% rock abundance and below 5% rock abundance. A – terminal part of the tongue; B – ablation area below icefalls; C – southern small cirque; D – southeastern section of the western accumulation zone; E – western accumulation zone above 3500 m.a.s.l. in 2013; F – the entire glacier’s area.

ablation zone ROI contains the tongue-terminal ROI within it. Therefore, the latter has a significant influence on the former leading to similarity of trend between them (Fig. 7B).

The small side-cirque and the retreating section of the western accumulation zone follow similar patterns of rock abundance increase (Fig. 7C, D). These areas show exposed

ice on large portions of the ROIs between 2013 and 2017. Afterwards, the range of rock abundances suddenly increases, accompanied by a rise in the medians (Fig. 7C, D). In the first half of the studied period the small side cirque has only up to 4.1% of pixels with more than 95% rock abundance and 65.2% of sub-2.5% pixels (Fig. 7C). By 2022 the share of

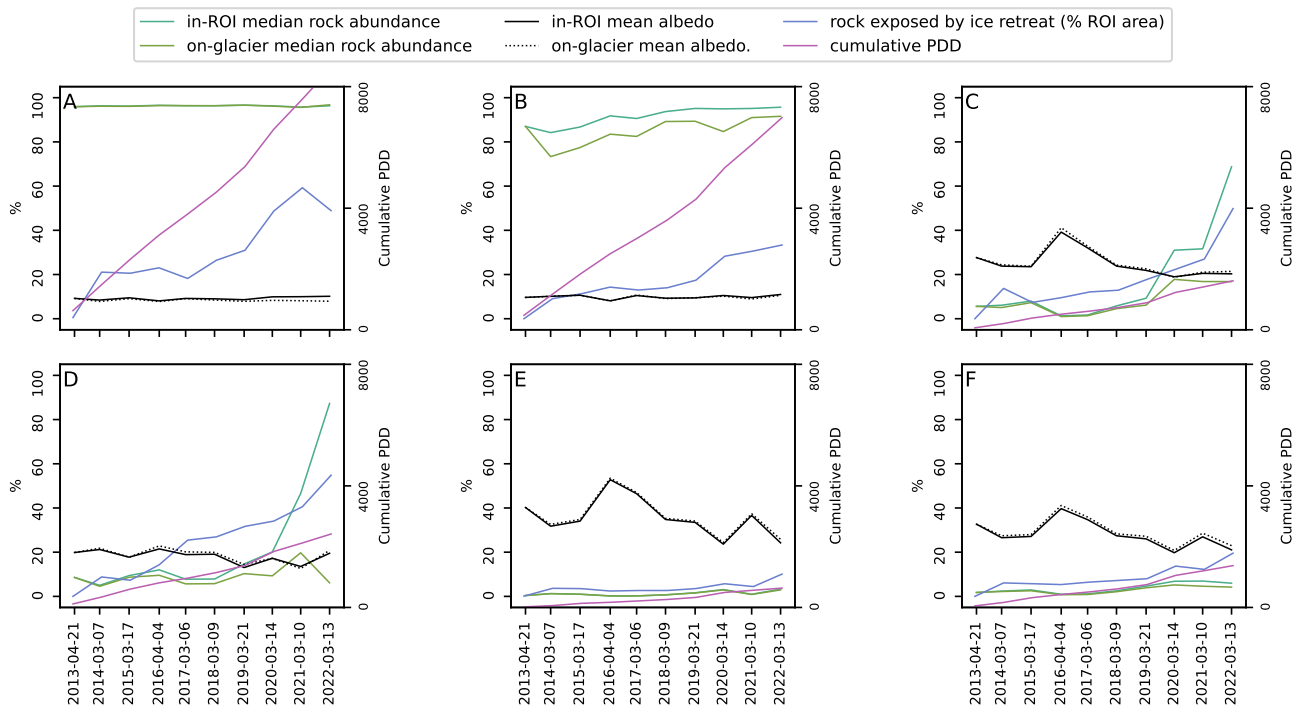


Figure 8: Results of multitemporal sediment coverage analysis. Timeseries of six parameters indicated in the legend at the top in the manually chosen ROI: A – terminal part of the tongue; B – ablation area below icefalls; C – southern small cirque; D – southeastern section of the western accumulation zone; E – western accumulation zone above 3500 m.a.s.l. in 2013; F – the entire glacier's area.

the most rocky pixels and drops to 13.8% in 2022 while the share of the least rocky ones rises to 27.6%. In the retreating section of the western accumulation zone the increase in rock abundance within the ROI is more gradual (Fig. 7D), with median staying below 20% until 2019 and then rising.

The western accumulation zone exhibits very low rock abundances throughout the studied period (Fig. 7E). The mean consistently exceeded the median, suggesting the presence of a small number of highly rocky pixels among the predominantly bright surface. The mean and median consistently lie below 20% with fluctuations similar to the smaller ROIs. Less than 4% of pixels are fully covered by debris (rock abundance >95%), while the share of pixels with rock abundance below 5% ranges from 65.9% to 86.8%.

The shapes of the boxplots of the entire glacier are most similar to those of the small cirque (Fig. 7F). While the range of rock abundance values is getting progressively wider starting in 2018, the median remains steadily below 20%. High-rock abundance pixels are relatively scarce, accounting for less than 7% in the first half of the studied period and gradually increasing up to 14.1% after 2016. Low-abundance pixels constitute a proportion of the overall population between 42.9% and 64.7%.

4.6. Retreat and sediment accumulation within ROIs

The median in-ROI rock abundance and median on-glacier rock abundance present varying trends between

ROIs, albeit on-glacier sediment cover and the share of rock exposed by glacial retreat increase across all ROIs and the entire glacier (Fig. 8). The in-ROI and on-glacier mean albedo signals are similar to each other in all ROIs and in all times. The glacier's tongue has low albedo with a slight divergence between in-ROI and on-glacier values in the lowest section (Fig. 3A,B). The remaining ROIs see gradual albedo decrease, with a singular uptick in 2016 (Fig. 3C-F), which is less pronounced in the receding section of the western ablation zone (Fig. 3D).

The ROIs covering the lowest part of the glacier present the highest median rock abundances, close to 100% in the smaller one, and an increasing trend above 80% in the larger one (Fig. 3A, B). The in-ROI and on-glacier rock abundances are relatively similar. Compared to the most terminal section, the sub-icefall zone with areas of exposed ice has lower proportion of on-glacier sediment. The median rock abundances remain high, which can be attributed to both the presence of sediment on the glacier surface or the shrinking of its boundary.

The receding sections of the glacier demonstrate how big impact the exposure of the bedrock by ice retreat has on the detected rock abundances. In the two cases outside of the tongue the in-ROI median rock abundance deviates from the on-glacier median rock abundance after 2020, indicating an acceleration of the ice retreat exposing greater area of bare rock within the ROIs (Fig. 8 C, D). In the receding part of the western accumulation zone the in-ROI detected rock

abundance timeseries corresponds more closely to the rate of retreat rather than to the rate of sediment accumulation (Fig. 8D). With low on-glacier median rock abundance throughout the study period, the changes detected by KBRI represent freshly exposed rocks. Contrastingly, the small cirque ROI shows increases in both on-glacier sediment share and the percentage of exposed rock (Fig. 8C). In this case, the in-ROI rock abundance is a combination of sediment accumulation and retreat.

The western ablation zone and the entire glacier ROIs show a steady increase in the median rock abundance (Fig. 8E, F). Within the entire glacier's 2013 outline the values of median rock abundance are moderated by the size of the area of aggregation (Fig. 8F). The recession and thick debris cover are confined to a small area relative to the entire glacier. Despite rapid changes in these areas they do not significantly distort data averaged over the entire glacier as the bulk of pixels fall over exposed ice and snow. Similarly, in the western accumulation zone the signal of an increase in rock abundance on the margins of the area is overshadowed by the large number of pixels with zero or near-zero rock abundances (Fig. 8E).

4.7. Relationship between rock abundance and albedo and meteorological variables

The albedo and glacier retreat or sediment accumulation are consistently negatively correlated, aligning with expectation of darkening of areas where exposed ice area shrinks or is covered by debris. These correlations are statistically significant in ROIs that do not have intensely retreating margins (Fig. 9C, E, F). The on-glacier rock abundance is the most consistently correlated there indicating that the albedo drop is connected to accumulation of debris. In the tongue ROIs and the receding part of the eastern accumulation zone the in-ROI and on-glacier albedo are not statistically significantly correlated with rock detection measures (Fig. 9A, B, D). The correlations between albedo and rock detection measures are also lower there.

The only statistically significant correlations in the receding part of the western accumulation zone are between annual and cumulative PDD and in-ROI rock detection measures (Fig. 9D). These correlation values are positive and high (between 0.67 and 0.99). The on-glacier rock abundance does not correlate significantly with any environmental measures indicating that in this ROI the changes in rock abundance are caused by ice margin retreat, not accumulation of debris.

Absolute correlation values are high and statistically significant across the board when calculated over the entire 2013 glacier extent (Fig 9F). PDD and cumulative PDD show a positive correlation with the measures of surface darkening, while mean albedo and sum of precipitation exhibit a negative correlations with the measures of surface darkening. These patterns are shared with the ROIs of western accumulation area and the small cirque (Fig 9C, E). The exception is that in the former of these two the cumulative PDD does not correlate significantly with the measures other

than the % of exposed bedrock. At the same time, the annual PDD does correlate highly and significantly with in-ROI and on-glacier median rock abundances signifying importance of snowfall variability for the accumulation zone.

4.8. Drainage network

Despite the clear evolution of the sediment cover, the properties of the glacier tongue drainage network appear to have remained unchanged between 2013 and 2022 (Fig. 10). The maps of potential stream density are similar to each other visually. The observed stream density across the area is around 0.05 to 0.25 m/m², reaching values as high as 0.33 m/m² in individual pixels. The 2013 map of stream density has faint outlines of ogives visible in the north-eastern part of the studied section, while the 2022 map shows faint ogive patterns lower down the tongue (Fig. 10A-B). On both maps from the respective years, noticeable sections of medial moraines can be observed at the end of the glacier's tongue and along the line where the two branches of the glacier meet. These sections appear as strips with lower potential stream density compared to the surrounding areas. In year 2022, the strip associated with the medial moraine extends further upglacier compared to its extent in 2013.

The change in stream density ranges between -0.1 and 0.1 m/m² on most of Universidad's tongue, with negative values prevalent in the western part of the lower tongue and below the western icefall. The eastern part of the lower tongue and the space below the confluence of Universidad's two trunks display the negative values (Fig. 10C). Increases higher than 0.1m/m² can be observed on isolated pixels in these areas and along a short, narrow strip at the confluence, with no values exceeding 0.22 m/m² of change. Decreases in potential stream density greater than 0.1 m/m² are also relatively rare but show a higher concentration compared to the pixels in the high increase range. The most significant decrease in stream density is observed on the eastern side of the confluence and in close proximity to the glacier's terminus, particularly along the medial moraine. However, the decrease in stream density does not exceed -0.30m/m² anywhere.

Maps of mean stream order tell a similar story of limited change during the years between 2013 and 2022 (Fig. 10C-E). The mean stream order within an L8 pixel across the tongue mostly falls between 1 and 2. Higher values can be observed along the banks of the medial moraines and ogives in 2013, as well as in scattered lines across the lower tongue in 2022. Notably, there is a disappearance of a pattern of high mean stream order on the western bank of the northern tributary, which is evident both by comparing the two snapshot maps (Fig. 10D-E) and by examining the map of differences (Fig. 10F). The latter demonstrates a trend of stable mean stream order, with few pixels showing an increase above 0.50, while decreases are visible along the medial moraines and the eastern edge of the tongue..

The spatial autocorrelation analysis generated a map revealing statistically significant clusters of similar behavior in the aggregated stream data. A region with a high density

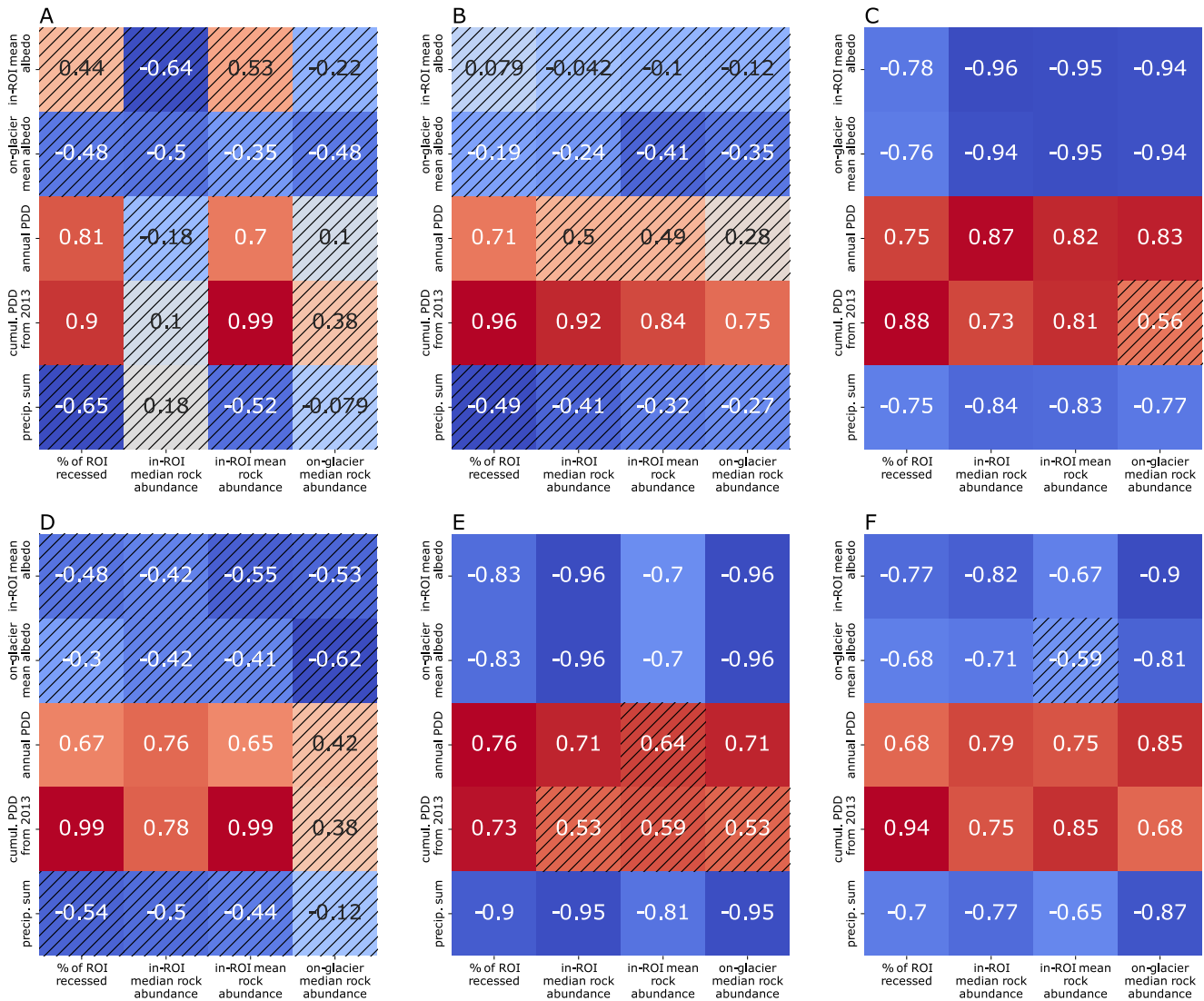


Figure 9: Correlation matrices between environmental variables and measures of rock abundance and recession in the selected ROIs. Hatched fields indicate statistically non-significant results. A – terminal part of the tongue; B – ablation area below icefalls; C – southern small cirque; D – southeastern section of the western accumulation zone; E – western accumulation zone above 3500 m.a.s.l. in 2013; F – the entire glacier’s area.

change is situated in the middle of the tongue and extends upwards towards the eastern tributary. Conversely, areas of minimal change in stream density coincide with highly crevassed regions below the western icefall and with areas in the eastern lobe of the lower tongue. Within all of these clusters, there are threads of opposite behavior. Notably, spots of high change are observed on sections of ice directly adjacent to the moraines, while in the high-change cluster, which generally exhibits limited debris cover, areas of low change align with the presence of moraines (Fig. 11C). On the map of stream order’s spatial correlation, the statistically significant clusters indicate an increase in the mean stream order in areas of exposed ice and a decrease in the measure on moraines (Fig. 11F).

The input datasets for the stream detection algorithm contained maps of sinks (wells) derived from both DEMs. The two datasets are, again, very close to each other in terms

of number of detected wells. On the area of the analysed part of the tongue in 2013 we have detected 696 wells, while in 2022 there were 690. This count includes sinks only within the 2022 glacier contour and excludes the heavily crevassed area in the highest part of the analysed area. The highly irregular topography in this area leads to the detection of numerous local depressions, but they don’t have a significant impact on the stream network outside of their immediate vicinity

5. Discussion

5.1. KBRI and darkening of the glacier

The values of KBRI over Universidad are consistently negative over both rock and ice. The lower values correspond to a lower rock abundance (sediment presence) in a pixel, but almost all pixels show negative KBRI regardless of the

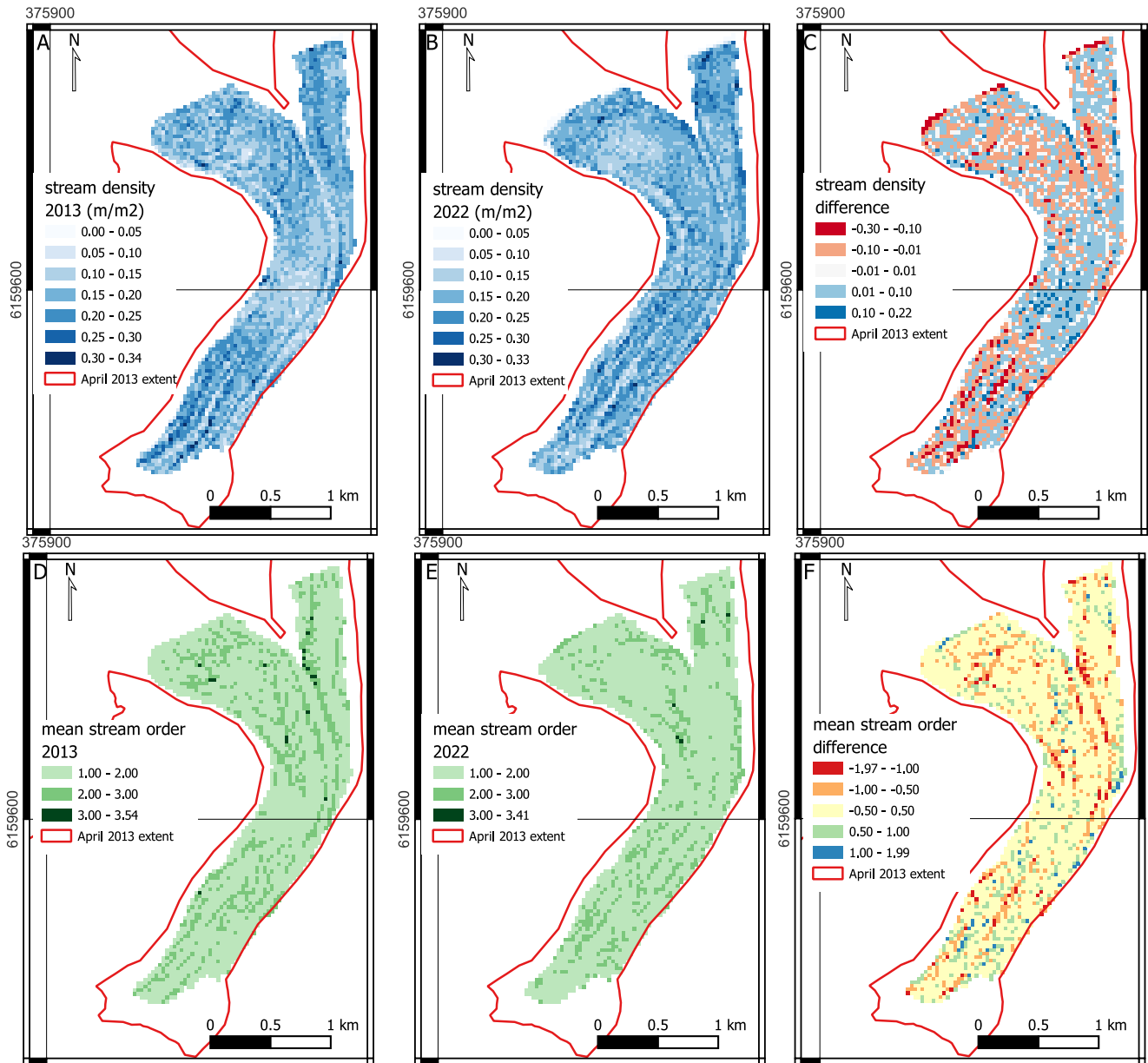


Figure 10: Maps of stream network properties and their changes. First row: potential stream density as modeled from A – 2013 LiDAR DEM; B – 2022 UAV DEM; C – difference between 2022 and 2013. Second row: mean potential stream order as modeled from D – 2013 LiDAR DEM, E – 2022 UAV DEM; F – difference between 2022 and 2013.

surface type. Pei et al. (2018), the authors of the index, obtained lower KBRI for pixels with low (< 15%) karst rock abundance than we did for pixels of low rock abundance. This is due to different non-rock surfaces in the two different cases: vegetation in the work of Pei et al. (2018), and ice in our study. Ice reflectance in the NIR band is usually higher than in the SWIR band, however the difference between the bands is significantly lower in case of dirty ice than in case of bright, clean ice (Naegeli et al., 2017). The reflectance of vegetation is also significantly higher in the NIR band than in both SWIR bands.

KBRI increases linearly with the increase of exposed bedrock, as described in the study by Pei et al. (2018), with KBRI values above zero observed in pixels with more

than 23.9% rock abundance. However, the KBRI values we obtained over exposed rock and moraine do not exceed 0 significantly, and KBRI=0 is found near 100% of rock abundance (Fig. 5). This discrepancy can be explained by different composition of the imaged rocks. The moraines of Universidad consist of granodiorite (Liboutry, 1958; Fernández et al., 2022), a type of felsic igneous rock, while the original study of Pei et al. (2018) analyzed karst (carbonate) rocks of Southern China (Pei et al., 2018). The karst rocks are characterized by a lower reflectance in NIR than in SWIR (Pei et al., 2018). The granodiorite spectral reflectance curve also exhibits NIR reflectance below SWIR reflectance, as reported by Cardoso-Fernandes et al. (2021) and Ghrefat et al. (2021). However, the difference between

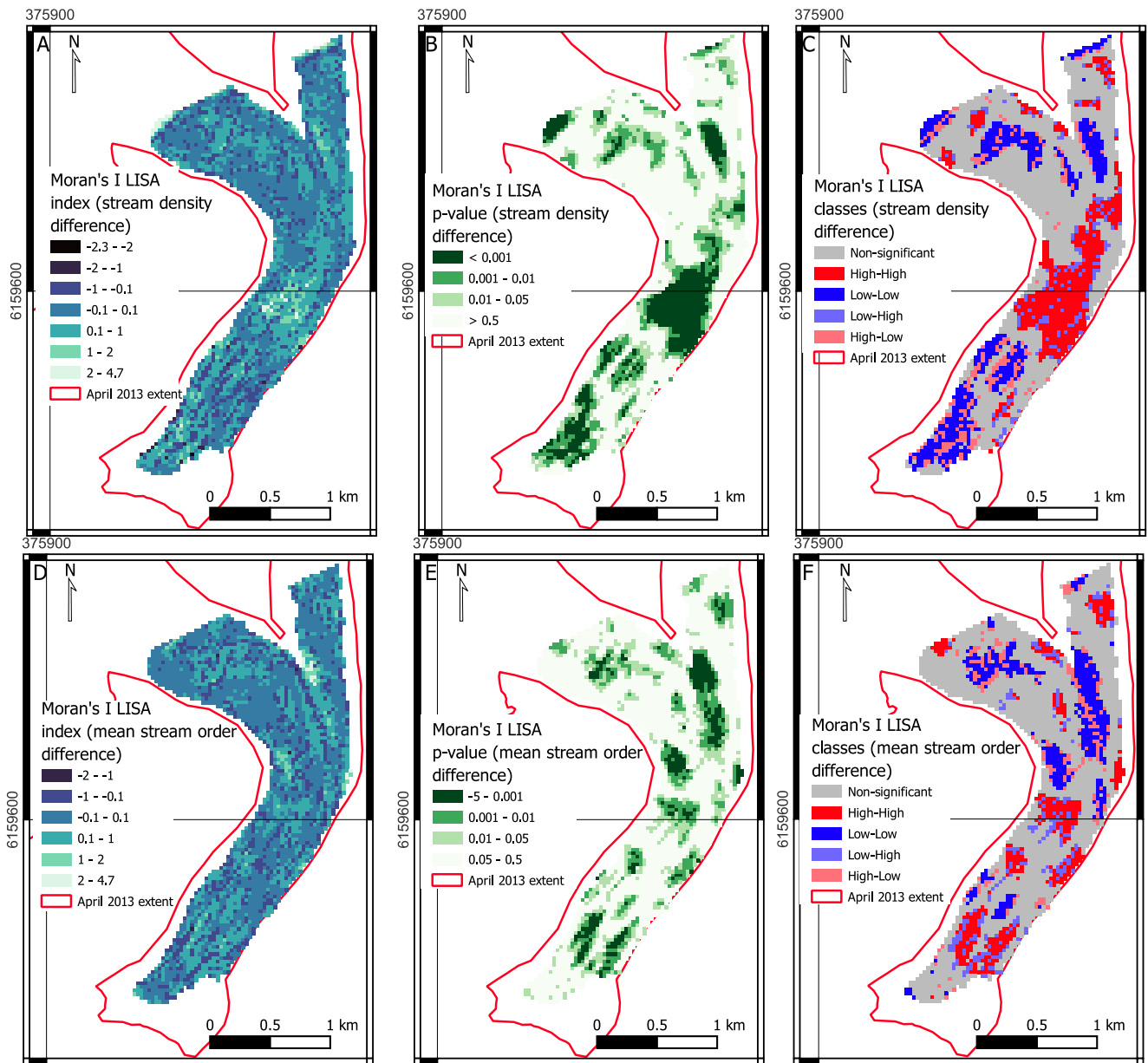


Figure 11: Results of Moran I autocorrelation analysis of the stream properties maps. Upper row (A, B, C) demonstrates results of work on the map of stream density difference, lower row (D, E, F) contains results of analyses of stream order difference. First column (A, D) is the map of the values of the local indicators of spatial association (LISA), middle column (B, E) maps areas of statistical significance of LISA and the third column visualises the data classified into five classes based on significance and relationship between a spot and its surroundings.

the two bands is lower compared to ice and lower than what was reported for karst by Pei et al. (2018).

The KBRI index is sensitive to the presence of rock material on the surface, allowing for the detection of both sediment cover overlaying the glacier surface and rocky areas exposed due to glacier recession. However, it does not distinguish between these two surface types. Therefore, KBRI can be valuable in determining the extent of ice- and snow-covered sections of glaciers, particularly in relation to efforts focused on tracking recession. This makes it comparable to other index-based glacier mapping approaches (Haireti et al., 2016; Bhardwaj et al., 2014; Fleischer et al., 2021).

Our comparison between KBRI and albedo highlights the advantage of KBRI in its ability to disregard variations in ice color. Through machine-learning-based classification of high-resolution multispectral imagery, we consistently observed the presence of exposed ice areas on the lower tongue of the glacier. However, these areas appeared very dark due to the presence of embedded sediments (Fig. 2). The KBRI maps, segmented using unsupervised machine learning, effectively capture this pattern, particularly in the eastern section of the tongue near the medial moraine (Fig. 6). The low correlation between albedo maps and rock abundance in the

terminal section of the glacier (Fig. 9A) supports this finding. The spectrally dark surface of sediment-contaminated ice reflects limited broadband radiation, but it appears distinct from the actual rock surface on a contrast-enhanced infrared index image.

5.2. Sediment accumulation and glacier's retreat

In the case of Universidad, the increasing rock abundance seen in the Landsat KBRI timeseries (Fig. 6C) results from a combination of glacier recession and sediment cover accumulation on the glacier. Different areas of the glacier are subject to ice margin retreat, sediment build-up or both of these processes at once. Similarly, the two phenomena contribute to gradual decrease of albedo on the scale of the entire glacier within its 2013 outline. Gradual exposure of the underlying rock by ice retreat, as well as accumulation of sediment, both lead to reduced reflection of incident radiation. In case of the revealed bedrock it means heating of the areas which were previously cold and subsequent transfer of the heat to the atmosphere with longwave radiation emitted by the rocks which leads to advection of heat onto the marginal parts of the glacier. This forms a localized feedback loop as increasingly revealed bedrock inputs increasing amount of energy which contributes to acceleration of melting and retreat.

Albedo measurements across entire glaciers are necessarily biased towards the albedo of the dominant surface type across this glacier (Naegeli et al., 2019), which in case of Universidad would be the bare ice surface. The majority of the accumulation area, as well as the ablation area above the debris-covered tongue and between moraines, expose glacial ice at the end of the ablation season. Changes such as ice margin retreat and debris cover expansion, in the case of Universidad, occur on a relatively small portion of the glacier. Spectral measurements taken from a limited number of pixels in rapidly changing areas are "diluted" by measurements taken from a larger number of pixels representing a consistent surface of glacial ice. The overall shape of the glacier's albedo timeseries resembles that of the western accumulation zone (Fig. 8 E, F), with dampened amplitude of values between years. Meanwhile, the percentage of revealed rock within the 2013 glacier outline (the whole glacier ROI) increases at a faster rate than within the ROI of the western accumulation area. As the rock abundance remains stable over the years in the accumulation zone ROI, we assume that the change in albedo is largely due to the disappearance of bright snow cover and the exposure of the darker ice beneath.

Another part of the glacier, located in the former accumulation zone, consists of two small ice cirques to the west of the main trunk of the Universidad glacier. These areas experience more dynamic changes compared to the larger accumulation zone. In 2013, the two areas were connected to the glacier's trunk through outlets, which transported masses of ice downstream. By February 2023, the two small cirques are visually disconnected from the glacier's trunk, although this does not necessarily mean a complete cut-off of ice supply from these sources. The continuous band of dark

sediment observed may actually be a thick layer of sediment, beneath which the glacier flow processes are still active. However, the risk of complete disconnection is not the only threat to these two ice bodies. Our mapping indicates a reduction in the extent of these ice areas along their entire perimeter, including in the highest parts (Fig. 3B). Ice margin retreat in this area has accelerated since 2019, leading to the complete cutoff from the main trunk in 2022. The year 2021 was the last year when snowpack was observed in those small cirques at the end of the ablation season (Fig. 3A). It is possible that low precipitation in the year leading up to April 2022 (Fig. 1C) and subsequent reduced surface runoff during the 2022 ablation season slowed down processes that could naturally wash down fresh debris from the ice surface. The on-glacier rock abundance detected in this ROI correlates more strongly with precipitation and annual PDD than with cumulative PDD, emphasizing the importance of short-term conditions for debris accumulation.

The correlations between climatological variables and the conditions on the glacier surface did not always exhibit statistical significance. Within different ROIs, different pairs of parameters show significance, further hinting at locally important processes. In the lowest part of the tongue, significance is observed only in the correlation between PDD and ice margin retreat. However, on the wider tongue, the on-glacier rock abundance also shows a significant correlation with cumulative PDD. The retreating part of the western accumulation zone demonstrates similar relationships, but notably, on-glacier rock abundance does not correlate significantly with any of the tested variables. This may mean that retreat may be the primary process impacting KBRI readings there – a justified assumption given that the in-ROI KBRI calculation include both on-glacier and off-glacier parts of the ROI. In the cases of the small accumulation cirque and the entire glacier's ROI, almost all correlations are statistically significant, testifying to the complexity of the occurring changes. Finally, in the western accumulation zone, the only non-significant correlations are those between cumulative PDD and rock abundances. This ROI is also the one with lowest rock abundances. This observation could suggest that precipitation and short-term temperature changes may play a more important role than long-term energy input in driving changes on the surface of the accumulation area.

5.3. Manual mapping and ELA estimates

Our delineation of the accumulation and ablation areas relies on manually drawn lines on high-resolution satellite imagery. The estimates of ELA and AAR based on these hand-drawn snow extents are inherently prone to errors and cannot be considered absolutely accurate. However, despite the relatively high standard deviation of elevations for the hand-drawn equilibrium lines (Table 2), the shift observed between 2013 and 2023 is several times larger than the standard deviation of the latter estimate. In other words, even under a conservative scenario where the 2023 ELA is overestimated by one standard deviation, we would still

observe an increase in ELA of over 300 meters. In the same interval, there was a drop in AAR from 0.68 to 0.10. This indicates that more than 80% of the 2013 accumulation area, corresponding to half of the glacier's surface, has transitioned from an accumulation regime to an ablation regime within the past 10 years. During the latter part of this period, between 2019 and 2023, we observe significant fluctuations in ELA ranging from approximately 3700 to 4100 m.a.s.l., as well as shifts in AAR oscillating between 0.48 and 0.04 (Fig. 4A). This period also exhibits oscillations in the albedo of the western accumulation area (Fig. 8E) and yearly precipitation sum, with the yearly PDD sum remaining relatively stable from 2020 to 2022 (Fig. 1C).

The snow line prior to the end of the ablation season on the two main accumulation areas reached 3500 m.a.s.l. in both 2015 and 2019 (Fig. 2A, B). In 2020, the detected snow cover reached the 3500 m.a.s.l. isoline at certain points (Fig. 2C). Areas where the snow cover on the map does not extend below this elevation are typically located along the mountain slopes, where deep shadows are present in the analyzed image. However, since the neighboring areas surrounding the shadows are also classified as bare ice, the absence of snow above 3500 m.a.s.l. cannot be attributed solely to a classification artifact caused by low reflectance in the shaded regions.

During the manual mapping of late season snowline extent, the examination of the Dove/RE-1 imagery showed patterns of snow cover reappearing in the same locations in years of more abundant snow cover, with bare ice in the same places in years of limited snowfall. This fluctuation led us to interpret the white, smooth areas on the imagery as pure snow without any firn surfaces. These areas were sometimes bright white, but often they appeared darker, indicating a thin layer of dust on top of the snow. The decrease in albedo observed in the accumulation area is a result of dust accumulation, shrinking snow cover, and retreat of the ice margin. Despite significant fluctuations in albedo over the years, the abundance of on-glacier rock remains stable. The strong correlation between albedo and dust cover suggests a synchronized trend between the two. This disparity in variability indicates another important factor influencing the situation in the Universidad's western accumulation zone: snow cover. In years of high precipitation, the snow covers the darker bare ice and sediment, while also helping to wash away accumulated dust with meltwater, thereby increasing the glacier's albedo. In drier years, the glacial ice and unhindered accumulation of dust contribute to a reduction in albedo as these two precipitation-dependent factors work together to darken the surface. This conceptual model aligns with a previous study on Chilean glaciers, which identified precipitation and snow cover as controlling factors of glaciers' albedo (Shaw et al., 2020). The low significance of the rock abundance-cumulative PDD correlation further supports the claim, that mass balance of Universidad Glacier is controlled in a larger part by interannual variations in snowfall than by temperature.

5.4. Hydrological situation

Significant changes in water-bearing facies in the upper regions of a glacier typically impact the hydrological conditions of glacier sections that drain the accumulation areas. However, in the case of the Universidad glacier, deep crevasses related to the icefalls at the outlets of the northern and western accumulation zones effectively capture water that flows downglacier from the accumulation zones. We hypothesize that this phenomenon mitigates the impact of water from the higher regions of the glacier on the hydrological conditions of the glacier tongue. Meltwater from the upper parts of the glacier drains into englacial and subglacial conduits through crevasses and moulins located at the outlets of the large cirques. As a result, the tongue of the glacier, situated below the icefalls, represents a distinct hydrological zone. With limited inflow from the upper regions of the glacier, precipitation, local snowmelt, and ice melting are the only significant sources of water on the glacier tongue.

Universidad glacier has experienced a lowering of its surface in the decade covered by the present work and in the preceding one. In the period 2010-2020, the glacier experienced a mean change of -1.65 m^{-1} , which accelerated to -2.07 m a^{-1} in the 2019-2020 interval (Hugonnet et al., 2021b,a). The change is likely stronger over the tongue, as implied from a comparison of 2000-2013 elevations (Podgórski et al., 2019). Therefore, we assume that the drainage system in the ablation area undergoes annual re-carving, as intensive melting modifies the preexisting topography every summer, coinciding with the formation of channels by the flowing water.

The similarity of stream network properties between 2013 and 2022 implies a comparable water supply to the system. Under the aforementioned assumptions, such a situation requires either that both precipitation and heat input were at similar levels in 2013 and 2022, or that any change in one factor is counterbalanced by an opposite change in the other. On the exposed ice areas, the properties of the drainage network remained relatively unchanged, including the number of moulins. Locally, statistically significant increases in stream density and stream order were observed over the ice, while these measures decrease over moraines. The decrease in mean stream order and stream density over moraines may result from reduced availability of water from precipitation. Insufficient rain or snowmelt in debris-covered areas inhibits the development of a dendritic network, resulting in drainage remaining confined to singular streams. Similarly, the increases observed over the exposed ice would imply an amplified water supply over these areas. Thus, the enhanced ice melt due to rising temperatures would exceed the water loss caused by reduced precipitation.

According to the data obtained from the ERA5-Land reanalysis (Fig. 1C), the cumulative precipitation in the 12 months leading up to 1 April 2013 was 1700 mm, while the corresponding period before 1 April 2022 shows a sum of 975 mm. This indicates that the precipitation value in 2022 is only 57% of the value observed in 2013. Regarding the cumulative PDD sum, the 12-month period leading up

to 1 April 2013 recorded a value of $381^{\circ}Cd$, whereas the same metric for the period before 1 April 2022 shows a value of $720^{\circ}Cd$. In this case, the PDD sum in 2022 is 189% of the value observed in 2013. When recalculated based on the mean elevation of the sub-icefall ROI, the 2022 PDD sum constitutes 178% of the 2013 PDD sum ($844^{\circ}Cd$ and $475^{\circ}Cd$, respectively). These numbers highlight the contrasting behavior of the two meteorological factors. The cooler year of 2013 experienced substantial precipitation, while the warmer year of 2022 was characterized by dry conditions.

This analysis takes into account only the two datapoints, years on two ends of our studied time period. However, the ERA5-Land time series shows fluctuating PDD and precipitation sums throughout the study period. Accordingly, the extent of snow cover in the accumulation zones also does fluctuate (Fig. 4A), as does the discharge in Tinguririca river (Fig. 4B). It is, however, important to note that the discharge in the river is also following the ENSO phases with higher discharge during the El Niño phases, which bring more precipitation, than the La Niña phases.

Bravo et al. (2017) estimated that during the summer 2009/10, Universidad glacier contributed between 4.3% and 19.5% of the water in the Tinguririca river, depending on the month and assumed melt factor. Modeling melt under different climate change scenarios indicated that the discharge from the Universidad meltwater stream is projected to reach its maximum around year 2040 and then gradually decrease until 2100 (Escanilla-Minchel et al., 2020). The decrease in precipitation due to climatic change is mentioned as the primary reason for the reduction of water flow in the stream, whereas the peak discharge is attributed to the melting ice from the glacier. Escanilla-Minchel et al. (2020) also discovered a clear seasonal distribution of water sources in the stream: precipitation in autumn, snow meltwater in spring, and glacial meltwater during the peak discharge in summer.

Another study suggests that the ongoing Chilean Mega-Drought serves as an analogue for the future conditions, with anthropogenic forcing driving steady decrease in precipitation in the region (Boisier et al., 2018). In particular, the trend will impact mostly the summer precipitation. Under such conditions, the contribution of glacier to streamflow, including rivers like Tinguririca, will become even more important for water availability during the summer season. On a broader scale, Kinnard et al. (2020) note a correlation between the mass balance of Guanaco glacier, located around 600 km north of Universidad, with the position of South Pacific Subtropical High. The expansion and migration of this high pressure system were identified as a reason behind the decline in precipitation in this part of South America. The positive correlation between the AAR and the ONI index of the previous winter aligns with the expectation of increased precipitation during El Niño years (van Dongen et al., 2022).

On the other hand, Barandun et al. (2022) highlight factors other than just the climatic forcing that affect the mass

balance of the Paloma Norte and Olivares Alfa glaciers, both located approximately 180 km north of Universidad. These glaciers suffer from the accumulation of dust on the snow and ice surface due to mobilization of dust from increasingly exposed soils and strip-mining operations. The darkening of the glaciers' surface intensifies melt. While there are no mines in the immediate vicinity of Universidad, the glacier is surrounded by non-vegetated, rocky slopes. Thus, it can be expected that the decrease in albedo of Universidad, similarly to the glaciers described by Barandun et al. (2022), will contribute to the amplification of melt.

6. Conclusions

Following the warming of the climate in the area during the mega-drought period, Universidad glacier has experienced local retreat of its margins and accumulation of debris on the tongue. The lower tongue of the glacier and certain sections of the accumulation area have experienced a reduction of the ice extent. Simultaneously, the debris accumulation across the glacier is uneven, with the upper limit of moraines on the tongue progressing upward, and the accumulation area being affected by an influx of a thin but detectable layer of dust. The deposition of dust occurs on the surface of ice and snow in the accumulation area, inversely proportional to the amount of annual precipitation. During dry years, debris accumulates unimpeded on the ice and snow surface. In wet years, the dark ice and debris are hidden under snow cover, and the thin dust layer gets washed away by meltwater. The minor cirques to the west of the glacier's primary trunk deviate from this cycle. In these areas, both debris accumulation and ice margin retreat have been consistent over the years, posing a potential risk of isolation from the main tongue by 2022-23. The persistent debris layer in these cirques contributes to their diminishing size, and there is a possibility of complete disappearance on the near-term.

Similar processes are observed at the tongue of the glacier, where the upper limit of the terminal moraine appears to progress upward, while debris accumulates on the surface of the ice in an irregular manner. At the same time, the retreat of the tongue's margin reveals the underlying rock in front of the glacier. A thick layer of debris on the lowest part of the glacier blurs the border between the surface of the glacier and that of the bedrock in medium-resolution imagery, while the edge of the glacier can still be discerned in high-resolution satellite images. This area sees the thickest layer of accumulated debris across the entire glacier. The thickness of accumulated material can potentially be significant enough to isolate certain parts of the glacier from atmospheric warming, although this study lacks measurements to confirm this statement. In the glacier's accumulation zone, the upward progression of the ELA exposes the surface of glacial ice, leading to the absence of seasonally exposed firn across the entire surface of the glacier by the year 2023. This exposed ice has a darker appearance compared to the snow, which consequently affects the glacier albedo.

Between 2013 and 2022, the Universidad glacier tongue saw local increase in stream mean order and density in areas of exposed ice, alongside decreases in these two parameters on moraines. These trends point to a significant increase in water flow on the ice surface from melting ice parallel to reduction of water input from precipitation which led to reduced drainage on exposed moraines. The trends are consistent with reanalysis-based meteorological history. However, it is important to note that precipitation and temperatures have exhibited fluctuations over time. While our results indicate visible trends, variations are observed in the extent of summer snow cover, resulting in fluctuations in the amount of water stored after each accumulation season and the volume of meltwater discharged from the glacier. Given the limited extent of the firn layer and the shrinking snow cover, melting of the Universidad's ice will constitute an increasingly higher percentage of the total meltwater from the glacier in the medium and long term

We have demonstrated that a Landsat spectral index originally designed for karst rock detection can be effectively utilized to track the reduction in exposed ice and snow area of a mountain glacier. By training a logistic model on a hyperspectral dataset, the KBRI values can be converted into fractional rock abundance within a pixel of a Landsat 8 OLI image. KBRI shows the capability to distinguish between darkening caused by the presence of rocky material and darkening caused by the exposure of glacial ice, indicating its superiority over albedo-based debris detection. However, it is worth noting that the index is not sensitive to differences between rock material accumulated on the surface of the glacier and the rocky surface exposed due to the retreat of the glacier's margin.

Conflicts of interest

The funders had no role in the design of the study; in the collection, analyses, or interpretation of data; in the writing of the manuscript, or in the decision to publish the results

Acknowledgements

This research was funded by the National Science Center (NCN) PRELUDIUM grant number 2020/37/N/ST10/02481. J.P. acknowledges partial support from the International Environmental Doctoral School associated with the Centre for Polar Studies at the University of Silesia in Katowice. M.P. acknowledges partial support from the Priority Research Area (Anthropocene) under the Strategic Programme Excellence Initiative at Jagiellonian University and from ANID through FONDECYT grant 1220978. The hyperspectral imagery and 2013 elevation data were acquired within a project from the Fondo de Innovación para la Competitividad del Ministerio de Economía, Fomento y Turismo, Gobierno de Chile (C.K., R.U.). A.F. acknowledges Fondecyt 1201429 and Anillo ACT210080. Article contains modified information from ERA5-Land model by

Copernicus Atmosphere Monitoring Service 2023. Landsat-8 OLI imagery used in this article courtesy of the U.S. Geological Survey

References

- Alevkayali, Ç., Yayla, O., Atayeter, Y., 2023. Monitoring and classification of karst rocky desertification with landsat 8 OLI images using spectral indices, multi-endmember spectral mixture analysis and support vector machine. *International Journal of Engineering and Geosciences* 8, 277–289. doi:10.26833/ijeg.1149738.
- Ali, A., Dunlop, P., Coleman, S., Kerr, D., McNabb, R.W., Noormets, R., 2023. Glacier area changes in Novaya Zemlya from 1986–89 to 2019–21 using object-based image analysis in Google Earth Engine. *Journal of Glaciology*, 1–12doi:10.1017/jog.2023.18.
- Anselin, L., 2018. A local indicator of multivariate spatial association: Extending geary's *c*. *Geographical Analysis* 51, 133–150. doi:10.1111/gean.12164.
- Anselin, L., Syabri, I., Kho, Y., 2006. GeoDa: An introduction to spatial data analysis. *Geographical Analysis* 38, 5–22. doi:10.1111/j.0016-7363.2005.00671.x.
- Ayala, Á., Fariás-Barahona, D., Huss, M., Pellicciotti, F., McPhee, J., Farinotti, D., 2020. Glacier runoff variations since 1955 in the Maipo River basin, in the semiarid Andes of central Chile. *The Cryosphere* 14, 2005–2027. doi:10.5194/tc-14-2005-2020.
- Baraer, M., Mark, B.G., McKenzie, J.M., Condom, T., Bury, J., Huh, K.I., Portocarrero, C., Gómez, J., Rathay, S., 2012. Glacier recession and water resources in Peru's Cordillera Blanca. *Journal of Glaciology* 58, 134–150. doi:10.3189/2012jog11j186.
- Barandun, M., Bravo, C., Grobety, B., Jenk, T., Fang, L., Naegeli, K., Rivera, A., Cisternas, S., Münster, T., Schwikowski, M., 2022. Anthropogenic influence on surface changes at the Olivares glaciers; Central Chile. *Science of The Total Environment* 833, 155068. doi:10.1016/j.scitotenv.2022.155068.
- Basnett, S., Kulkarni, A.V., Bolch, T., 2013. The influence of debris cover and glacial lakes on the recession of glaciers in Sikkim Himalaya. *Journal of Glaciology* 59, 1035–1046. doi:10.3189/2013jog12j184.
- Benn, D., Evans, D.J.A., 2010. *Glaciers and Glaciation*. Routledge. 2nd edition, (Hodder Arnold Publication).
- Bhardwaj, A., Joshi, P.K., Snehamani, Singh, M.K., Sam, L., Gupta, R., 2014. Mapping debris-covered glaciers and identifying factors affecting the accuracy. *Cold Regions Science and Technology* 106–107, 161–174. doi:10.1016/j.coldregions.2014.07.006.
- Blaschke, T., Hay, G.J., Kelly, M., Lang, S., Hofmann, P., Addink, E., Feitosa, R.Q., van der Meer, F., van der Werff, H., van Coillie, F., Tiede, D., 2014. Geographic Object-Based Image Analysis – Towards a new paradigm. *ISPRS Journal of Photogrammetry and Remote Sensing* 87, 180–191. doi:10.1016/j.isprsjprs.2013.09.014.
- Boisier, J.P., Alvarez-Garretón, C., Cordero, R.R., Damiani, A., Gallardo, L., Garreaud, R.D., Lambert, F., Ramallo, C., Rojas, M., Rondanelli, R., 2018. Anthropogenic drying in central-southern Chile evidenced by long-term observations and climate model simulations. *Elementa: Science of the Anthropocene* 6. doi:10.1525/elementa.328.
- Bosson, J.B., Huss, M., Osipova, E., 2019. Disappearing World Heritage Glaciers as a Keystone of Nature Conservation in a Changing Climate. *Earth's Future* 7, 469–479. doi:10.1029/2018ef001139.
- Bravo, C., Loriaux, T., Rivera, A., Brock, B.W., 2017. Assessing glacier melt contribution to streamflow at Universidad Glacier, central Andes of Chile. *Hydrol. Earth Syst. Sci.* 21, 3249–3266. doi:10.5194/hess-21-3249-2017.
- Brun, F., Wagnon, P., Berthier, E., Jomelli, V., Maharjan, S.B., Shrestha, F., Kraaijenbrink, P.D.A., 2019. Heterogeneous Influence of Glacier Morphology on the Mass Balance Variability in High Mountain Asia. *Journal of Geophysical Research: Earth Surface* 124, 1331–1345. doi:10.1029/2018jfg004838.
- Campello, R.J.G.B., Moulavi, D., Sander, J., 2013. Density-based clustering based on hierarchical density estimates, in: *Advances in Knowledge*

- Discovery and Data Mining. Springer Berlin Heidelberg, pp. 160–172. doi:10.1007/978-3-642-37456-2_14.
- Cardoso-Fernandes, J., Silva, J., Perrotta, M.M., Lima, A., Teodoro, A.C., Ribeiro, M.A., Dias, F., Barrès, O., Cauzid, J., Roda-Robles, E., 2021. Interpretation of the Reflectance Spectra of Lithium (Li) Minerals and Pegmatites: A Case Study for Mineralogical and Lithological Identification in the Fregeneda-Almendra Area. *Remote Sensing* 13, 3688. doi:10.3390/rs13183688.
- Cathles, L.M., Abbot, D.S., Bassis, J.N., MacAyeal, D.R., 2011. Modeling surface-roughness/solar-ablation feedback: application to small-scale surface channels and crevasses of the greenland ice sheet. *Annals of Glaciology* 52, 99–108. URL: <https://doi.org/10.3189/172756411799096268>, doi:10.3189/172756411799096268.
- Chen, R.C., Dewi, C., Huang, S.W., Caraka, R.E., 2020. Selecting critical features for data classification based on machine learning methods. *Journal of Big Data* 7. doi:10.1186/s40537-020-00327-4.
- Crabbé, A.H., Somers, B., Roberts, D.A., Halligan, K., Dennison, P., Dudley, K., 2020. MESMA QGIS Plugin (Version 1.0.8) [Software]. Available from <https://bitbucket.org/kul-reseco/mesma>.
- DigitalGlobe, 2016. WorldView-2 Data Sheet and Core imagery product guide. <https://dg-cms-uploads-production.s3.amazonaws.com/uploads/document/file/98/WorldView2-DS-WV2-rev2.pdf>. Accessed: 2020-04-09.
- van Dongen, R., Scherler, D., Wendi, D., Deal, E., Mao, L., Marwan, N., Meier, C.I., 2022. El Niño Southern Oscillation (ENSO)-induced hydrological anomalies in central Chile doi:10.5194/egusphere-2022-1234.
- Dussailant, I., Berthier, E., Brun, F., Masiokas, M., Hugonnet, R., Favier, V., Rabatel, A., Pitte, P., Ruiz, L., 2019. Two decades of glacier mass loss along the Andes. *Nature Geoscience* 12, 802–808. doi:10.1038/s41561-019-0432-5.
- Escanilla-Minchel, R., Alcayaga, H., Soto-Alvarez, M., Kinnard, C., Urrutia, R., 2020. Evaluation of the Impact of Climate Change on Runoff Generation in an Andean Glacier Watershed. *Water* 12, 3547. doi:10.3390/w12123547.
- Falaschi, D., Berthier, E., Belart, J.M.C., Bravo, C., Castro, M., Durand, M., Villalba, R., 2022. Increased mass loss of glaciers in Volcán Domuyo (Argentinian Andes) between 1962 and 2020, revealed by aerial photos and satellite stereo imagery. *Journal of Glaciology* 69, 40–56. doi:10.1017/jog.2022.43.
- Falvey, M., Garreaud, R.D., 2009. Regional cooling in a warming world: Recent temperature trends in the southeast Pacific and along the west coast of subtropical South America (1979–2006). *Journal of Geophysical Research* 114. doi:10.1029/2008jd010519.
- Fernández, H., García, J.L., Nussbaumer, S.U., Geiger, A.J., Gärtner-Roer, I., Pérez, F., Tikhomirov, D., Christl, M., Egli, M., 2022. De-icing landsystem model for the Universidad Glacier (34° S) in the Central Andes of Chile during the past ~660 years. *Geomorphology* 400, 108096. doi:10.1016/j.geomorph.2021.108096.
- Fernández-Navarro, H., García, J.L., Nussbaumer, S.U., Tikhomirov, D., Pérez, F., Gärtner-Roer, I., Christl, M., Egli, M., 2023. Fluctuations of the Universidad Glacier in the Andes of central Chile (34°S) during the latest Holocene derived from a ¹⁰Be moraine chronology. *Quaternary Science Reviews* 300, 107884. doi:10.1016/j.quascirev.2022.107884.
- Fleischer, F., Otto, J.C., Junker, R.R., Hölbling, D., 2021. Evolution of debris cover on glaciers of the Eastern Alps, Austria, between 1996 and 2015. *Earth Surface Processes and Landforms* 46, 1673–1691. doi:10.1002/esp.5065.
- Fountain, A.G., Walder, J.S., 1998. Water flow through temperate glaciers. *Reviews of Geophysics* 36, 299–328.
- Gao, B.c., 1996. NDWI—A normalized difference water index for remote sensing of vegetation liquid water from space. *Remote Sensing of Environment* 58, 257–266. doi:10.1016/s0034-4257(96)00067-3.
- Garreaud, R.D., Boisier, J.P., Rondanelli, R., Montecinos, A., Sepúlveda, H.H., Veloso-Aguila, D., 2019. The Central Chile Mega Drought (2010–2018): A climate dynamics perspective. *International Journal of Climatology* 40, 421–439. doi:10.1002/joc.6219.
- Ghrefat, H., Kahal, A.Y., Abdelrahman, K., Alfaiifi, H.J., Qaysi, S., 2021. Utilization of multispectral landsat-8 remote sensing data for lithological mapping of southwestern Saudi Arabia. *Journal of King Saud University - Science* 33, 101414. doi:10.1016/j.jksus.2021.101414.
- Gorelick, N., Hancher, M., Dixon, M., Ilyushchenko, S., Thau, D., Moore, R., 2017. Google Earth Engine: Planetary-scale geospatial analysis for everyone. *Remote Sensing of Environment* doi:10.1016/j.rse.2017.06.031.
- Haireti, A., Tateishi, R., Alsaadeh, B., Gharechelou, S., 2016. Multi-criteria technique for mapping of debris-covered and clean-ice glaciers in the shaksgam valley using landsat TM and ASTER GDEM. *Journal of Mountain Science* 13, 703–714. doi:10.1007/s11629-015-3649-9.
- Haralick, R.M., Shanmugam, K., Dinstein, I.H., 1973. Textural features for image classification. *IEEE Transactions on systems, man, and cybernetics*, 610–621.
- Hock, R., 2005. Glacier melt: a review of processes and their modelling. *Progress in Physical Geography: Earth and Environment* 29, 362–391. doi:10.1191/0309133305pp453ra.
- Hugonnet, R., McNabb, R., Berthier, E., Menounos, B., Nuth, C., Girod, L., Farinotti, D., Huss, M., Dussailant, I., Brun, F., Kääb, A., 2021a. Accelerated global glacier mass loss in the early twenty-first century. *Nature* 592, 726–731. URL: <https://doi.org/10.1038/s41586-021-03436-z>, doi:10.1038/s41586-021-03436-z.
- Hugonnet, R., McNabb, R., Berthier, E., Menounos, B., Nuth, C., Girod, L., Farinotti, D., Huss, M., Dussailant, I., Brun, F., Kääb, A., 2021b. Accelerated global glacier mass loss in the early twenty-first century - Dataset. URL: <https://www.sedoo.fr/theia-publication-products?uuid=c428c5b9-df8f-4f86-9b75-e04c778e29b9>, doi:10.6096/13.
- Irvine-Fynn, T., Hubbard, B., 2016. Glacier hydrology and runoff, in: Richardson, D., Castree, N., Goodchild, M.F., Kobayashi, A., Liu, W., Marston, R.A. (Eds.), *International Encyclopedia of Geography*. Wiley. doi:10.1002/9781118786352.
- Janke, J.R., Bellisario, A.C., Ferrando, F.A., 2015. Classification of debris-covered glaciers and rock glaciers in the Andes of central Chile. *Geomorphology* 241, 98–121. doi:10.1016/j.geomorph.2015.03.034.
- Jones, D.B., Harrison, S., Anderson, K., Whalley, W.B., 2019. Rock glaciers and mountain hydrology: A review. *Earth-Science Reviews* 193, 66–90. doi:10.1016/j.earscirev.2019.04.001.
- Karszenberg, D., Schmitz, O., Salamon, P., de Jong, K., Bierkens, M.F., 2010. A software framework for construction of process-based stochastic spatio-temporal models and data assimilation. *Environmental Modelling & Software* 25, 489–502. doi:10.1016/j.envsoft.2009.10.004.
- Kim, Y., Kim, S., Jeong, H., An, H., 2022. Quantitatively defining megadrought based on drought events in central Chile. *Geomatics, Natural Hazards and Risk* 13, 975–992. doi:10.1080/19475705.2022.2060763.
- Kinnard, C., Ginot, P., Surazakov, A., MacDonell, S., Nicholson, L., Patris, N., Rabatel, A., Rivera, A., Squeo, F.A., 2020. Mass Balance and Climate History of a High-Altitude Glacier, Desert Andes of Chile. *Frontiers in Earth Science* 8. doi:10.3389/feart.2020.00040.
- Kinnard, C., MacDonell, S., Petlicki, M., Mendoza Martinez, C., Abermann, J., R. Urrutia, 2018. Mass balance and meteorological conditions at Universidad Glacier, Central Chile., in: Rivera, D.A., Godoy-Faundez, A., Saavedra, M.L. (Eds.), *Andean Hydrology*. CRC Press, Boca Raton, US. chapter 5, pp. 102–126.
- Li, J., Sheng, Y., 2012. An automated scheme for glacial lake dynamics mapping using Landsat imagery and digital elevation models: a case study in the Himalayas. *International Journal of Remote Sensing* 33, 5194–5213. doi:10.1080/01431161.2012.657370.
- Liang, S., 2001. Narrowband to broadband conversions of land surface albedo I. *Remote Sensing of Environment* 76, 213–238. doi:10.1016/s0034-4257(00)00205-4.
- Llibouty, L., 1958. Studies of the Shrinkage After a Sudden Advance, Blue Bands and Wave Ogives on Glacier Universidad (Central Chilean Andes). *Journal of Glaciology* 3, 261–270. doi:10.3189/s00221430002390x.
- Lu, Y., Zhang, Z., Huang, D., 2020. Glacier Mapping Based on Random Forest Algorithm: A Case Study over the Eastern Pamir. *Water* 12, 3231. doi:10.3390/w12113231.
- Malmros, J.K., Mernild, S.H., Wilson, R., Yde, J.C., Fensholt, R., 2016. Glacier area changes in the central Chilean and Argentinian Andes 1955–2013/14. *Journal of Glaciology* 62, 391–401. doi:10.1017/jog.

2016. 43.
- Mark, B.G., Baraer, M., Fernandez, A., Immerzeel, W., Moore, R.D., Weingartner, R., 2015. Glaciers as water resources, in: *The High-Mountain Cryosphere*. Cambridge University Press, pp. 184–203. doi:10.1017/cbo9781107588653.011.
- Masiokas, M.H., Rabatel, A., Rivera, A., Ruiz, L., Pitte, P., Ceballos, J.L., Barcaza, G., Soruco, A., Bown, F., Berthier, E., Dussailant, I., MacDonell, S., 2020. A Review of the Current State and Recent Changes of the Andean Cryosphere. *Frontiers in Earth Science* 8. doi:10.3389/feart.2020.00099.
- McCarthy, M., Meier, F., Fatichi, S., Stocker, B.D., Shaw, T.E., Miles, E., Dussailant, I., Pellicciotti, F., 2022. Glacier Contributions to River Discharge During the Current Chilean Megadrought. *Earth's Future* 10. doi:10.1029/2022ef002852.
- McInnes, L., Healy, J., 2017. Accelerated hierarchical density based clustering, in: *Data Mining Workshops (ICDMW), 2017 IEEE International Conference on*, IEEE. pp. 33–42.
- McNabb, R.W., Womble, J.N., Prakash, A., Gens, R., Haselwimmer, C.E., 2016. Quantification and Analysis of Icebergs in a Tidewater Glacier Fjord Using an Object-Based Approach. *PLOS ONE* 11, e0164444. doi:10.1371/journal.pone.0164444.
- Milner, A.M., Khamis, K., Battin, T.J., Brittain, J.E., Barrand, N.E., Füreder, L., Cauvy-Fraunié, S., Gíslason, G.M., Jacobsen, D., Hannah, D.M., Hodson, A.J., Hood, E., Lencioni, V., Ólafsson, J.S., Robinson, C.T., Tranter, M., Brown, L.E., 2017. Glacier shrinkage driving global changes in downstream systems. *Proceedings of the National Academy of Sciences* 114, 9770–9778. doi:10.1073/pnas.1619807114.
- Mitkari, K.V., Arora, M.K., Tiwari, R.K., 2017. Extraction of Glacial Lakes in Gangotri Glacier Using Object-Based Image Analysis. *IEEE Journal of Selected Topics in Applied Earth Observations and Remote Sensing* 10, 5275–5283. doi:10.1109/jstars.2017.2727506.
- Muñoz-Sabater, J., 2019. Era5-land hourly data from 2001 to present. URL: <https://cds.climate.copernicus.eu/doi/10.24381/cds.e2161bac>, doi:10.24381/CDS.E2161BAC. (Accessed on 29.11.2022).
- Naegeli, K., Damm, A., Huss, M., Wulf, H., Schaepman, M., Hoelzle, M., 2017. Cross-Comparison of Albedo Products for Glacier Surfaces Derived from Airborne and Satellite (Sentinel-2 and Landsat 8) Optical Data. *Remote Sensing* 9, 110. doi:10.3390/rs9020110.
- Naegeli, K., Huss, M., Hoelzle, M., 2019. Change detection of bare-ice albedo in the Swiss Alps. *The Cryosphere* 13, 397–412. doi:10.5194/tc-13-397-2019.
- NASA/METI/AIST/Japan Spacesystems And U.S./Japan ASTER Science Team, 2019. Aster global digital elevation model v003. URL: <https://lpdaac.usgs.gov/products/astgtmv003/>, doi:10.5067/ASTER/ASTGTM.003.
- NOAA, 2023. Cold and warm episodes by season. URL: https://origin.cpc.ncep.noaa.gov/products/analysis_monitoring/ensostuff/ONI_v5.php, accessed on 18.06.2023.
- Oerlemans, J., Giesen, R., Broeke, M.V.D., 2009. Retreating alpine glaciers: increased melt rates due to accumulation of dust (Vadret da Morteratsch, Switzerland). *Journal of Glaciology* 55, 729–736. doi:10.3189/002214309789470969.
- östrem, G., 1959. Ice Melting under a Thin Layer of Moraine, and the Existence of Ice Cores in Moraine Ridges. *Geografiska Annaler* 41, 228–230. URL: <https://doi.org/10.1080/20014422.1959.11907953>, doi:10.1080/20014422.1959.11907953.
- Pei, J., Wang, L., Huang, N., Geng, J., Cao, J., Niu, Z., 2018. Analysis of Landsat-8 OLI Imagery for Estimating Exposed Bedrock Fractions in Typical Karst Regions of Southwest China Using a Karst Bare-Rock Index. *Remote Sensing* 10, 1321. doi:10.3390/rs10091321.
- Pitcher, L.H., Smith, L.C., 2019. Supraglacial streams and rivers. *Annual Review of Earth and Planetary Sciences* 47, 421–452. URL: <https://doi.org/10.1146/annurev-earth-053018-060212>, doi:10.1146/annurev-earth-053018-060212.
- Podgórski, J., Kinnard, C., Pełlicki, M., Urrutia, R., 2019. Performance Assessment of TanDEM-X DEM for Mountain Glacier Elevation Change Detection. *Remote Sensing* 11, 187. doi:10.3390/rs11020187.
- Podgórski, J., Pełlicki, M., 2020. Detailed Lacustrine Calving Iceberg Inventory from Very High Resolution Optical Imagery and Object-Based Image Analysis. *Remote Sensing* 12, 1807. doi:10.3390/rs12111807.
- Pu, J., Zhao, X., Dong, P., Wang, Q., Yue, Q., 2021. Extracting Information on Rocky Desertification from Satellite Images: A Comparative Study. *Remote Sensing* 13, 2497. doi:10.3390/rs13132497.
- Rastner, P., Bolch, T., Notarnicola, C., Paul, F., 2014. A Comparison of Pixel- and Object-Based Glacier Classification With Optical Satellite Images. *IEEE Journal of Selected Topics in Applied Earth Observations and Remote Sensing* 7, 853–862. doi:10.1109/jstars.2013.2274668.
- Richter, R., Schläpfer, D., 2017. *Atmospheric / topographic correction for airborne imagery: ATCOR-4 User Guide*.
- Roberts, D., Gardner, M., Church, R., Ustin, S., Scheer, G., Green, R., 1998. Mapping Chaparral in the Santa Monica Mountains Using Multiple Endmember Spectral Mixture Models. *Remote Sensing of Environment* 65, 267–279. doi:10.1016/s0034-4257(98)00037-6.
- Robson, B.A., Nuth, C., Dahl, S.O., Hölbling, D., Strozzi, T., Nielsen, P.R., 2015. Automated classification of debris-covered glaciers combining optical, SAR and topographic data in an object-based environment. *Remote Sensing of Environment* 170, 372–387. doi:10.1016/j.rse.2015.10.001.
- Ruan, O., Liu, S., Zhou, X., Luo, J., Hu, H., Yin, X., Yuan, N., 2023. LANDSAT multispectral image analysis of bedrock exposure rate in highly heterogeneous karst areas through mixed pixel decomposition considering spectral variability. *Land Degradation & Development* 34, 2880–2895. doi:10.1002/ldr.4654.
- Ryan, J.C., Hubbard, A., Stibal, M., Irvine-Fynn, T.D., Cook, J., Smith, L.C., Cameron, K., Box, J., 2018. Dark zone of the greenland ice sheet controlled by distributed biologically-active impurities. *Nature Communications* 9. URL: <https://doi.org/10.1038/s41467-018-03353-2>, doi:10.1038/s41467-018-03353-2.
- Sales, V.F., Zanutta, D.C., Jr., A.M., Racolte, G., Muller, M., Cazarin, C.L., Ibanez, D., Jr., L.G., Veronez, M.R., 2023. An adaptive spectral index for carbonate rocks using OLI Landsat-8 imagery. *Geocarto International* 38. doi:10.1080/10106049.2023.2179671.
- Schaaf, C., 2009. *Terrestrial Essential Climate Variables*. GTOS Essential Climate Variable Reports. Food and Agriculture Organization of the United Nations, Rome. Available online: <http://www.fao.org/3/a-i0197e.pdf>. Accessed on 30.05.2020.
- Selmes, N., Murray, T., James, T.D., 2011. Fast draining lakes on the Greenland Ice Sheet. *Geophysical Research Letters* 38. doi:10.1029/2011gl047872.
- Shaw, T.E., Ulloa, G., Fariás-Barahona, D., Fernandez, R., Lattus, J.M., McPhee, J., 2020. Glacier albedo reduction and drought effects in the extratropical Andes, 1986–2020. *Journal of Glaciology* 67, 158–169. doi:10.1017/jog.2020.102.
- Shokory, J.A.N., Lane, S.N., 2023. Patterns and drivers of glacier debris-cover development in the Afghanistan Hindu Kush Himalaya. *Journal of Glaciology*, 1–15doi:10.1017/jog.2023.14.
- Slangen, A.B.A., Adloff, F., Jevrejeva, S., Leclercq, P.W., Marzeion, B., Wada, Y., Winkelmann, R., 2016. A Review of Recent Updates of Sea-Level Projections at Global and Regional Scales. *Surveys in Geophysics* 38, 385–406. doi:10.1007/s10712-016-9374-2.
- Smith, L.C., Chu, V.W., Yang, K., Gleason, C.J., Pitcher, L.H., Rennermalm, A.K., Legleiter, C.J., Behar, A.E., Overstreet, B.T., Moustafa, S.E., Tedesco, M., Forster, R.R., LeWinter, A.L., Finnegan, D.C., Sheng, Y., Balog, J., 2015. Efficient meltwater drainage through supraglacial streams and rivers on the southwest Greenland Ice Sheet. *Proceedings of the National Academy of Sciences* 112, 1001–1006. doi:10.1073/pnas.1413024112.
- Trimble Geospatial, 2017. *Trimble eCognition Suite for Windows operating system*.
- Urrutia-Jalabert, R., Barichivich, J., Szejner, P., Rozas, V., Lara, A., 2023. Ecophysiological Responses of *Nothofagus obliqua* Forests to Recent Climate Drying Across the Mediterranean-Temperate Biome Transition in South-Central Chile. *Journal of Geophysical Research: Biogeosciences* 128. doi:10.1029/2022jg007293.
- Valdés-Pineda, R., Pizarro, R., García-Chevesich, P., Valdés, J.B., Olivares, C., Vera, M., Balocchi, F., Pérez, F., Vallejos, C., Fuentes, R., Abarza, A., Helwig, B., 2014. Water governance in Chile: Availability, management

- and climate change. *J. Hydrol.* 519, 2538–2567. doi:10.1016/j.jhydro1.2014.04.016.
- Vaughan, D., Comiso, J., Allison, I., Carrasco, J., Kaser, G., Kwok, R., Mote, P., Murray, T., Paul, F., Ren, J., Rignot, E., Solomina, O., Steffen, K., Zhang, T., 2013. Observations: Cryosphere., in: *Climate Change 2013: The Physical Science Basis. Contribution of Working Group I to the Fifth Assessment Report of the Intergovernmental Panel on Climate Change.* Cambridge University Press, Cambridge, United Kingdom and New York, NY, USA.
- Venegas-González, A., Muñoz, A.A., Carpintero-Gibson, S., González-Reyes, A., Schneider, I., Gipolou-Zuñiga, T., Aguilera-Betti, I., Roig, F.A., 2022. Sclerophyllous Forest Tree Growth Under the Influence of a Historic Megadrought in the Mediterranean Ecoregion of Chile. *Ecosystems* 26, 344–361. doi:10.1007/s10021-022-00760-x.
- Vincent, C., Wagnon, P., Shea, J.M., Immerzeel, W.W., Kraaijenbrink, P., Shrestha, D., Soruco, A., Arnaud, Y., Brun, F., Berthier, E., Sherpa, S.F., 2016. Reduced melt on debris-covered glaciers: investigations from Changri Nup Glacier, Nepal. *The Cryosphere* 10, 1845–1858. doi:10.5194/tc-10-1845-2016.
- Wessels, R.L., Kargel, J.S., Kieffer, H.H., 2002. ASTER measurement of supraglacial lakes in the Mount Everest region of the Himalaya. *Annals of Glaciology* 34, 399–408.
- Wyatt, F.R., Sharp, M.J., 2015. Linking surface hydrology to flow regimes and patterns of velocity variability on Devon Ice Cap, Nunavut. *Journal of Glaciology* 61, 387–399. doi:10.3189/2015jog14j109.
- Xie, F., Liu, S., Wu, K., Zhu, Y., Gao, Y., Qi, M., Duan, S., Saifullah, M., Tahir, A.A., 2020. Upward Expansion of Supra-Glacial Debris Cover in the Hunza Valley, Karakoram, During 1990 ~ 2019. *Frontiers in Earth Science* 8. doi:10.3389/feart.2020.00308.
- Yang, K., Smith, L.C., 2013. Supraglacial Streams on the Greenland Ice Sheet Delineated From Combined Spectral–Shape Information in High-Resolution Satellite Imagery. *IEEE Geoscience and Remote Sensing Letters* 10, 801–805. doi:10.1109/lgrs.2012.2224316.
- Yousuf, B., Shukla, A., Arora, M.K., Bindal, A., Jasrotia, A.S., 2020. On Drivers of Subpixel Classification Accuracy—An Example From Glacier Facies. *IEEE Journal of Selected Topics in Applied Earth Observations and Remote Sensing* 13, 601–608. doi:10.1109/jstars.2019.2955955.
- Zemp, M., Huss, M., Thibert, E., Eckert, N., McNabb, R., Huber, J., Barandun, M., Machguth, H., Nussbaumer, S.U., Gärtner-Roer, I., Thomson, L., Paul, F., Maussion, F., Kutuzov, S., Cogley, J.G., 2019. Global glacier mass changes and their contributions to sea-level rise from 1961 to 2016. *Nature* 568, 382–386. doi:10.1038/s41586-019-1071-0.